Hydrothermal niobium (Nb) mineralization and mobilization in the world-class Madeira Sn-Nb-Ta granitic deposit (Amazonas, Brazil)

Quentin Bollaert, Mathieu Chassé, Artur Bastos Neto, Adriana Horbe, Thierry Allard, Nicolas Menguy, Corentin Le Guillou, Alexandra Courtin, Cécile Quantin, Delphine Vantelon, et al.

Ore Geology Reviews 174 (2024) 106321

Contents lists available at ScienceDirect

Ore Geology Reviews

journal homepage: www.elsevier.com/locate/oregeorev

Hydrothermal niobium (Nb) mineralization and mobilization in the world-class Madeira Sn-Nb-Ta granitic deposit (Amazonas, Brazil)

Quentin Bollaert [a,*], Mathieu Chassé [a], Artur Bastos Neto [b], Adriana Horbe [c], Thierry Allard [a], Nicolas Menguy [a], Corentin Le Guillou [d], Alexandra Courtin [e], Cécile Quantin [e], Delphine Vantelon [f], David Troadec [g], Laurence Galoisy [a], Georges Calas [a]

[a] Sorbonne Université, Institut de Minéralogie, de Physique des Matériaux et de Cosmochimie, 4 place Jussieu, Paris, 75005, France
[b] Instituto de Geociências, Universidade Federal do Rio Grande do Sul, Porto Alegre, Brazil
[c] Instituto de Geociências, Universidade de Brasilia, Brazil
[d] Université de Lille, CNRS, INRAE, ENSCL, UMR 8207 - UMET - Unité Matériaux et Transformations, F-59000 Lille, France
[e] Géosciences Paris-Saclay (GEOPS), UMR 8148 Université Paris-Saclay – CNRS, 91405 Orsay Cedex, France
[f] Synchrotron SOLEIL, L'Orme des Merisiers, Départementale 128, 91190 Saint-Aubin, France
[g] Institut d'Electronique, de Microélectronique et de Nanotechnologies, Université de Lille, CNRS, Université Polytechnique Hauts-de-France, UMR 8520–IEMN, F-59000 Lille, France

ARTICLE INFO

Keywords:
Niobium mineralization
Pitinga
Pyrochlore
Columbite
Hydrothermal alteration
Mobilization
Uraninite

ABSTRACT

The Madeira deposit is a world-class tin (Sn) deposit characterized by a unique mineralogical assemblage composed of a massive cryolite ($NaAlF_3$) deposit associated with economically important metals like Nb (0.20 wt % Nb_2O_5). Although hydrothermal alteration has long been recognized in the cryolite formation, its effects on the mineralization and mobility of Nb remain obscure. This study presents new data on the Nb mineralization of the Pitinga core and border albite-enriched granites provided by nanoscale and site-selective approaches, using transmission electron microscopy and synchrotron-radiation analyses. Pyrochlore is the main Nb ore mineral with three distinct compositional types (U-Pb, Pb-U and Y-bearing varieties). Hydrothermal processes lead to the extensive alteration of pyrochlore into columbite (later designated as columbitization) by a coupled dissolution-reprecipitation mechanism, which evidences the alterability of pyrochlore in a hydrothermal context. Nanoscale analyses of veins and reaction interfaces reveal the presence of additional Nb hosts including fergusonite-(Y), Nb-bearing uraninite and Nb-bearing coffinite which formed from the alteration of pyrochlore. The nature of the altered phases mainly depends on the composition of the parent pyrochlore. Their formation, occurring in absence of direct proximity with remaining pyrochlore, shows that Nb mobilization at macroscopic scale is possible in F-rich reducing fluids. Niobium L_3-edge XANES spectroscopy on bulk samples representative of the different facies show that hydrothermal processes change the Nb mineralization by converting primary U-Pb-bearing pyrochlore into columbite and Pb-U/Y-bearing pyrochlores. The columbitization process of pyrochlore led to the increase of the Nb ore grade. Nonetheless, hydrothermal alteration modified Nb mineral liberation, thereby limiting the recovery of the full range of Nb host phases.

1. Introduction

Niobium is a critical metal which integrates the component of high strength low alloy steels (HSLA), superalloys as well as energy-related technologies (Schulz et al., 2017). The demand of Nb, which has quadrupled between 2000 and 2022, may increase even more in case of utilization in Li batteries to improve their storage rates (Griffith et al., 2018). Over 90 % of Nb production results from the recovery of the pyrochlore-mineral supergroup [$A_2Nb_2O_6(O,OH,F)$] from Brazilian laterites which formed over carbonatite lithotypes (e.g., Araxá and Catalão-I) (Braga and Biondi, 2023; Cordeiro et al., 2011). Due to its economic importance and its capacity to record geological processes (Walter et al., 2018; Velásquez-Ruiz et al., 2024) most recent research focused on pyrochlores from carbonatites and associated laterites (Giovannini et al., 2020; Khan et al., 2021; Ribeiro da Costa et al., 2021; Zaitsev et al., 2021; Palmieri et al., 2022; Ying et al., 2023; Bollaert

* Corresponding author.
E-mail address: qbollaert@me.com (Q. Bollaert).

https://doi.org/10.1016/j.oregeorev.2024.106321
Received 9 July 2024; Received in revised form 28 October 2024; Accepted 29 October 2024
Available online 31 October 2024

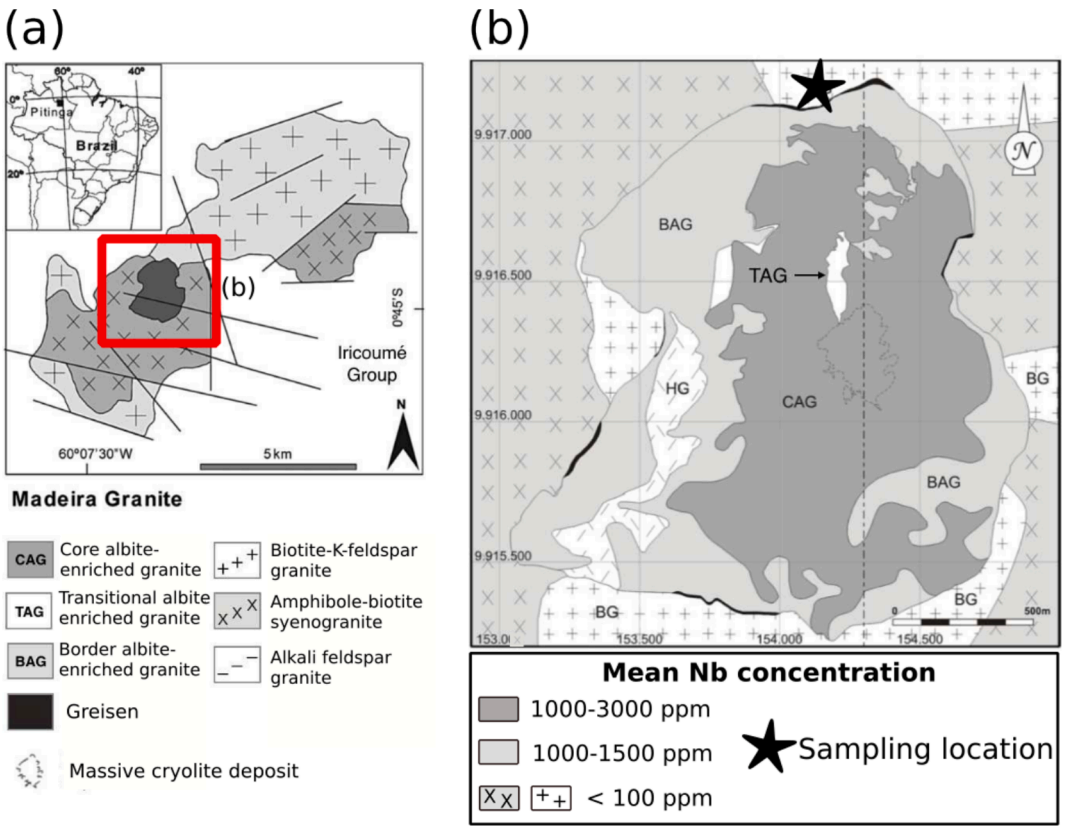

Fig. 1. (a) Location and geological map of the Madeira granite (modified after Costi et al., 2000). (b) Geological map of the albite-enriched granite facies (modified after Minuzzi et al., 2005). Average Nb concentrations are from Costi, (2000). The black star indicates the location of sampling of the BAG and CAG, which were transported 50–100 m north due to a dynamite blast.

et al., 2023a; Zhu et al., 2024; Velásquez-Ruiz et al., 2024). Pyrochlore is also an economically viable ore phase in granitic-syenitic systems (Salvi et al., 2005; Yong et al., 2022).

However, pyrochlore does not only account for Nb mineralization in most deposits. Each Nb occurrence is unique with respect to the degree of hydrothermal alteration and replacement by other minerals (Mitchell, 2015). Hydrothermal alteration of the Saint-Honoré carbonatite (Canada) has led to the transformation of pyrochlore into columbite-(Fe) ($[Fe,Mn]Nb_2O_6$) (Tremblay et al., 2017). Dolomitization of the Aley carbonatite (Canada) has resulted in the alteration of pyrochlore into a complex paragenesis including euxenite ($[Y,Ca,Ce,U,Th][Nb,Ta,Ti]_2O_6$), fersmite ($[Ca, Ce, Na][Nb, Ta, Ti]_2[O, OH, F]_6$), columbite-(Fe) and Nb-rich rutile (Chakhmouradian et al., 2015). In the Nechalacho deposit, extensive hydrothermal alteration resulted in the formation of Nb-bearing zircon, and U-bearing columbite formed from pyrochlore (Timofeev and Williams-Jones, 2015). Despite the evident influence of hydrothermal processes on the nature of secondary Nb minerals, it is still unclear whether metasomatic processes contribute to the development of Nb enrichment beyond the initial levels controlled by magmatic stages (Ying et al., 2023).

The majority of Nb occurrences shows only a relatively minor influence of hydrothermal processes on Nb enrichment (Finch et al., 2019; Van Lichtervelde et al., 2017; Wu et al., 2021) or comparable to magmatic concentration processes (Wang et al., 2021; Zhao et al., 2021; Yin, 2023). This limited contribution is attributed to the immobility of Nb during fluid-rock interactions, a consequence of its low solubility in diluted aqueuous fluids (Yajima, 1994; Peiffert et al., 2010) and the intrinsic resistance of Nb minerals to alteration (Lumpkin and Ewing, 1995). However, there is growing evidence that Nb can be mobilized by hydrothermal fluids at a micron scale only, due to its reprecipitation as secondary minerals (Sheard et al., 2012; Deditius et al., 2015; Timofeev and Williams-Jones, 2015; Wu et al., 2021; Williams-Jones and Vasyukova, 2022). These studies showed that fluorine plays a key role in significantly increasing Nb solubility (Timofeev et al., 2015; Lukyanova et al., 2017; Akinfiev et al., 2020). This trend is expected from Hard-Soft-Acid-Base theory which states that hard acids like Nb^{5+} form water soluble complexes with hard anions like F^- (Pearson, 1963). The solubility was shown to reach 3 wt% in 2 mol/kg HF aqueous solutions (Kotova, 2012; Timofeev et al., 2015; Liu et al., 2024). Such elevated F concentrations may better represent certain hydrothermal conditions, as indicated by mineral geofluorimeter studies estimating HF concentrations as high as 1 mol/kg in Ta-Nb-bearing granites (Aksyuk, 2002). The solubility, and therefore the mobility of Nb in F-rich fluids as found in hydrothermal context is likely underestimated. Despite experimental evidence of extensive Nb mobilization in subduction zone (Gao et al., 2007) and at the Earth's surface (Friis and Casey, 2018; Bollaert et al., 2023a), widespread Nb mobilization by hydrothermal processes have not yet been evidenced.

This paper investigates the hydrothermal Nb mineralization and mobilization in the albite-enriched Madeira Sn-bearing granitic world-class deposit (0.17 wt% Sn). In addition to Sn, the Madeira granite contains significant concentration of Nb (0.20 wt% Nb_2O_5) and Ta (0.024 wt% Ta_2O_5) hosted in U-Pb-bearing pyrochlore and columbite (Bastos Neto et al., 2009). The association of these economic metals with a massive cryolite (Na_3AlF_6) deposit formed from hydrothermal processes is unique in the world. The combination of intense alteration and high Nb and F enrichments make the albite-enriched Madeira granite an optimal candidate for exploring the effect of F-rich hydrothermal events on the mineralization and mobilization of Nb. Building on the foundational work of Bastos Neto et al. (2009), which first described and interpreted the hydrothermal Nb mineralization in Madeira, this study aims to demonstrate the value of advanced spectroscopic and

Table 1
Major and trace elements composition of the BAG and CAG samples obtained from ICP-OES and ICP-MS analyses.

wt%	Border-albite enriched facies	Core albite-enriched facies
SiO_2	66.47	64.29
Al_2O_3	14.22	14.06
Fe_2O_3	4.68	3.26
MnO	0.022	0.047
MgO	< L.D.	< L.D.
CaO	1.64	< L.D.
Na_2O	5.34	8.41
K_2O	4.30	4.50
TiO_2	0.026	0.037
P_2O_5	0.10	< L.D.
L.O.I.	1.46	3.66
Total	98.27	98.26
ppm		
As	8.16	3.51
Ba	34.4	6.5
Ga	84.9	66.1
Hf	228	235
Nb	**1597**	**1262**
Pb	619	598
Rb	2093	4781
Sc	4.85	2.32
Sn	2080	2936
Ta	280	200
Th	749	571
U	412	393
W	27.9	7.19
Y	1027	80.6
Zn	2803	1369
Zr	2400	3525
La	61.6	19.6
Ce	204	85.9
Pr	22.5	10.5
Nd	56.2	27.5
Sm	25.3	12.0
Eu	0.609	0.216
Gd	32.3	9.52
Tb	18.1	3.96
Dy	198	35.2
Ho	57.6	8.66
Er	212	30.8
Tm	40.3	6.13
Yb	254	45.3
Lu	31.3	6.53

microscopic tools in understanding the hydrothermal formation of Nb deposits. This study also complements previous investigations on Sn, U, and Th mineralizations in the Madeira granites (Costi et al., 2000; Hadlich et al., 2019; Hadlich, 2023), as well as Nb mineralization in lateritic profiles formed from the Madeira granites (Bollaert et al., 2023b; da S. Alves et al., 2018; Horbe and da Costa, 1999).

Here, the combined use of spatially-resolved chemical techniques at the micron and nanometric scales and X-ray absorption spectroscopy (XAS) reveals the complex Nb mineralization that resulted from the hydrothermal alteration of pyrochlore. Furthermore, the quantification of the average Nb speciation of the albite-enriched granites indicates that the extensive hydrothermal formation of columbite has led to the enhancement of the Nb ore grade, while degrading the mineral liberation.

2. Materials and methods

2.1. Geological context of the samples

The Madeira granite (Fig. 1) is the main Sn deposit in Brazil located in the northern part of the Amazonian Craton, part of the Paleoproterozoic Iricoumé Group (Lenharo et al., 2003). Four main facies have been distinguished based on their mineralogical and geochemical differences: the albite-enriched granite, biotite and alkali feldspars granite, amphibole and biotite syenogranite, and hypersolvus alkali feldspar granite (Costi, 2000). The albite-enriched facies is subdivided into the core albite-enriched granite (CAG) and border albite-enriched granite (BAG). These facies have a peralkaline composition and are characterized by Nb concentrations ranging from ca. 1000 to 3000 ppm (Costi, 2000). The CAG granite is also known to host a massive 10 million tons cryolite deposit at the center of the core facies (Fig. 1) whose formation is attributed to hydrothermal processes (Bastos Neto et al., 2009). The CAG and BAG samples were collected at the bottom of the weathering profile formed from the biotite-K-feldspar facies indicated by a black star (Fig. 1). The studied BAG and CAG samples were transported by a dynamite blast and can be considered allochtonous. The representativity of the samples is discussed in the Supplementary Material.

2.2. Bulk geochemical characterization

Two grams representative of CAG and BAG samples were sent to SARM (CRPG, Vandoeuvre-lès-Nancy) for bulk chemical elemental analysis. The concentrations of major and minor elements were obtained using an ICP-OES (Icap6500 ThermoFisher) and an ICP-MS (iVapQ ThermoFisher), respectively, after a Li tetraborate fusion (Carignan et al., 2001). The concentration of Nb is 1597 and 1262 ppm in the BAG and CAG samples, respectively. The concentration of major and minor elements concentrations is reported in Table 1. Analytical errors for major, minor and trace elements can be requested by contacting the SARM at https://sarm.cnrs.fr.

2.3. Microscale mineralogical analysis

After preparation of thin sections, the Nb minerals were characterized by scanning electron microscopy (SEM) equipped with a field emission electron gun (FEG) (Zeiss Ultra55, Sorbonne Université) operating at 15 kV. Semi-quantitative chemical data were obtained using a Bruker Quantax energy dispersive X-ray spectroscopy (EDS) system coupled to SEM using an Oxford 30 mm^2 silicon drift detector (SDD).

Mineral maps were obtained using the HyperSpy package (De la Peña et al., 2022) The background and X-ray lines of the SEM–EDS maps were fitted by a least-squares optimization algorithm (Zanetta et al., 2019). The signal was then denoised by a principal component analysis (PCA) algorithm in order to select the components explaining most variance of the data. Mean EDS spectra of the phases were obtained by selecting areas from the principal component decomposition and averaging the spectra within these areas. Owing to the small size of mineral phases, a subsequent linear least-squares fit was performed in order to unravel phase mixing at the pixel scale, where each pixel is fitted into a linear combination of the mean EDS spectra of the identified phases. Mineral maps were extracted by keeping the most abundant phase of each pixel.

Quantitative chemical data were obtained with electron probe microanalysis (EPMA) using a CAMECA SXFive EPMA equipped with five wavelength-dispersive spectrometers (WDS) at the Centre d'Analyse des Minéraux de Paris (CAMPARIS). Major and minor elements of pyrochlore and columbite grains from the BAG facies were analyzed using an accelerating potential of 15 keV and a sample current of 40nA and 299nA, respectively. The following standards were used: prehnite for Ca, $MnTiO_3$ for Mn and Ti, albite for Na, galena for Pb, cassiterite for Sn, monazite for Th, uraninite for U, zircon for Zr, for allanite-(Y) Y, La, Ce, allanite-(Nd) for Nd and Sm, orthoclase for Al, Fe_2O_3 for Fe, $LiNbO_3$ for Nb, metallic Ta for Ta, and garnet for Si.

2.4. Nanoscale mineralogical analysis

A focused ion beam (FIB) GFEI Strata Dual Beam 235 (Institute of Electronics, Microelectronics, and Nanotechnology) was used to extract

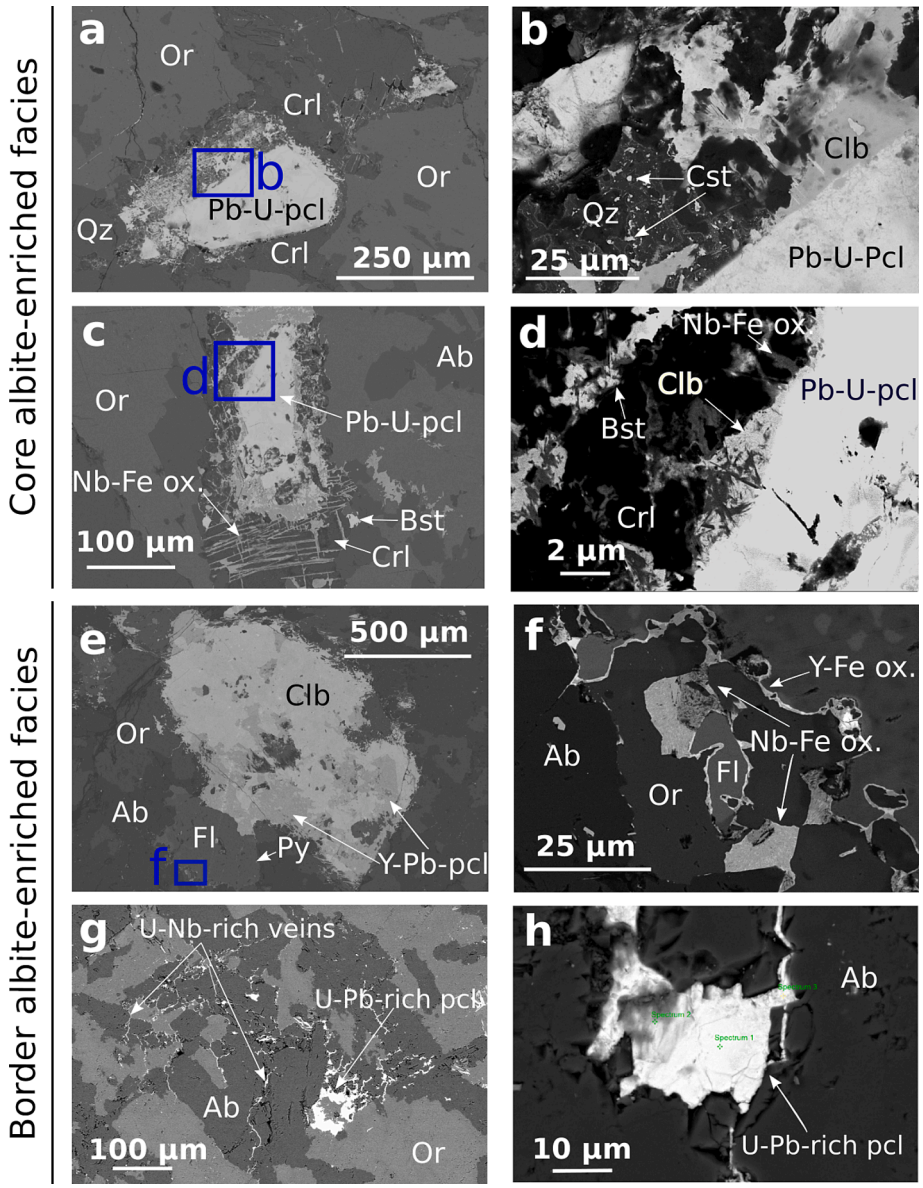

Fig. 2. Petrological observation of the Nb mineralization in the (a-d) CAG and (e-h) BAG lithotypes. (a) Crystal of Pb-U-bearing pyrochlore (Pcl) in orthoclase (Or) overgrown by cryolite (Crl). The top border displays heterogeneous corroded zone composed of (b) overgrowing columbite (Clb) and cassiterite (Cst). (c) Corroded pyrochlore replaced by cryolite, Fe oxides and bastnaesite (Bst). (d) Close-up view on the border of pyrochlore revealing the presence of micrometric-scale columbite. (e) Pseudomorph of columbite after Y-Pb-bearing pyrochlore. Fluorite is crosscut by Y-Nb-Fe-bearing veins which are also found at its border (f). (g-h) Uranium-Pb-bearing pyrochlore in BAG with U-bearing veins extending outwards pyrochlore.

mixed Nb-bearing phases that could not be identified using the resolution of SEM. Three FIB sections with of a size of 20 x 8 µm2 and a thickness of 100 nm were prepared. A Thermo Fisher ScientificTM Titan Themis transmission electron microscope (TEM) operated at 300 keV was used for chemical mapping in scanning transmission electron microscopy (STEM-EDS) at the University of Lille (UMET). Images that highlight variations in chemical density were obtained using a high-angle annular dark-field (HAADF) detector. The acquisition of EDX maps was performed using the super-X detector system, a current of 800 pA and a dwell time per pixel of 2 µs. Hyperspectral data processing was conducted using the Hyperspy software (De la Peña et al., 2022). Summation of pixels was performed to derive a signal-to-noise ratio for the identification of mineral phases. EDS spectra were acquired by selecting zones directly from the hyperspectral maps. For particularly heterogeneous or nanoscale-sized Nb-rich areas, EDS spectra were obtained by applying thresholds on the intensity of the Nb signal. RGB color chemical maps were generated using the 'plot_RGB_map' function integrated into Hyperspy.

A JEOL 2100F TEM (Sorbonne Université, IMPMC, Paris) was also used for the acquisition of high-resolution transmission electron microscopy (HR-TEM) images and selected area electron diffraction (SAED) patterns. Mineral identification was performed by measuring of interplanar spacings on the diffraction patterns using the TEM suite implemented on Image J software.

2.5. *X-ray absorption spectroscopy (XAS)*

2.5.1. *Data collection*

X-ray absorption spectra were collected at SOLEIL synchrotron facility (Saint-Aubin, France) operating with a storage ring current of 450 mA and an energy of 2.75 GeV on the LUCIA beamline (Vantelon et al., 2016). A Si(111) double-crystal monochromator was used with an energy resolution of 0.25 eV at 2400 eV (Schaefers et al., 2007). The monochromator was calibrated at the energy of the Nb L_3-edge using a

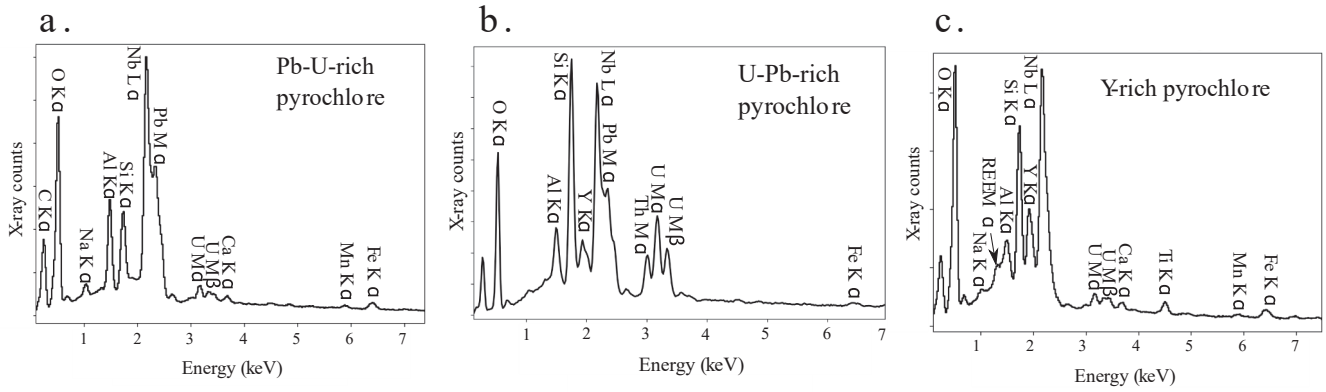

Fig. 3. SEM-EDS spectra obtained from the three compositional endmembers of pyrochlore present in the Pitinga granite. (a) Pb-U-bearing pyrochlore. (b) U-Pb-bearing pyrochlore. (c) Y-bearing pyrochlore. The majority of EDS spectra exhibit intermediate compositions between these three endmembers (Table 2).

Nb_2O_5 powder pellet at 2400 eV. X-ray Absorption Near Edge Structure (XANES) spectra were collected in fluorescence mode with energy steps of (2, 0.2, 1) eV for energy ranges of (2300–2350), (2350–2400) and (2400–2455) eV, respectively, with 1 s integration time. Two measurements per sample at room temperature and under primary vacuum were sufficient to get adequate signal-to-noise ratio and check for reproducibility of the edge features.

Bulk XANES were acquired on albite-enriched granites and mineralogical references while on thin sections of the albite-enriched granites samples, μ-XANES analysis was performed. First, elemental distribution were mapped by X-ray micro-fluorescence with an excitation energy of 2450 eV and a micro-beam focus of 2.8 x 3.8 μm to locate the Nb-rich regions of interest identified by SEM–EDS. From five to ten μ-XANES spectra of pre-identified minerals were then summed.

2.5.2. *Niobium speciation analysis*

Micro-XANES spectra collected in the CAG and BAG samples were compared to a set of natural and synthetic reference materials: fluorcalciopyrochlore, hydropyrochlore, Ba-bearing kenopyrochlore, U-bearing oxynatropyrochlore, columbite-(Mn), columbite-(Fe), and Nb-bearing hematite. Pyrochlore samples were provided by the mineral collection of Sorbonne Université. The U-rich oxynatropyrochlore corresponds to the sample numbered 214 investigated in Lumpkin and Ewing, (1995). Columbite samples were provided by École Nationale

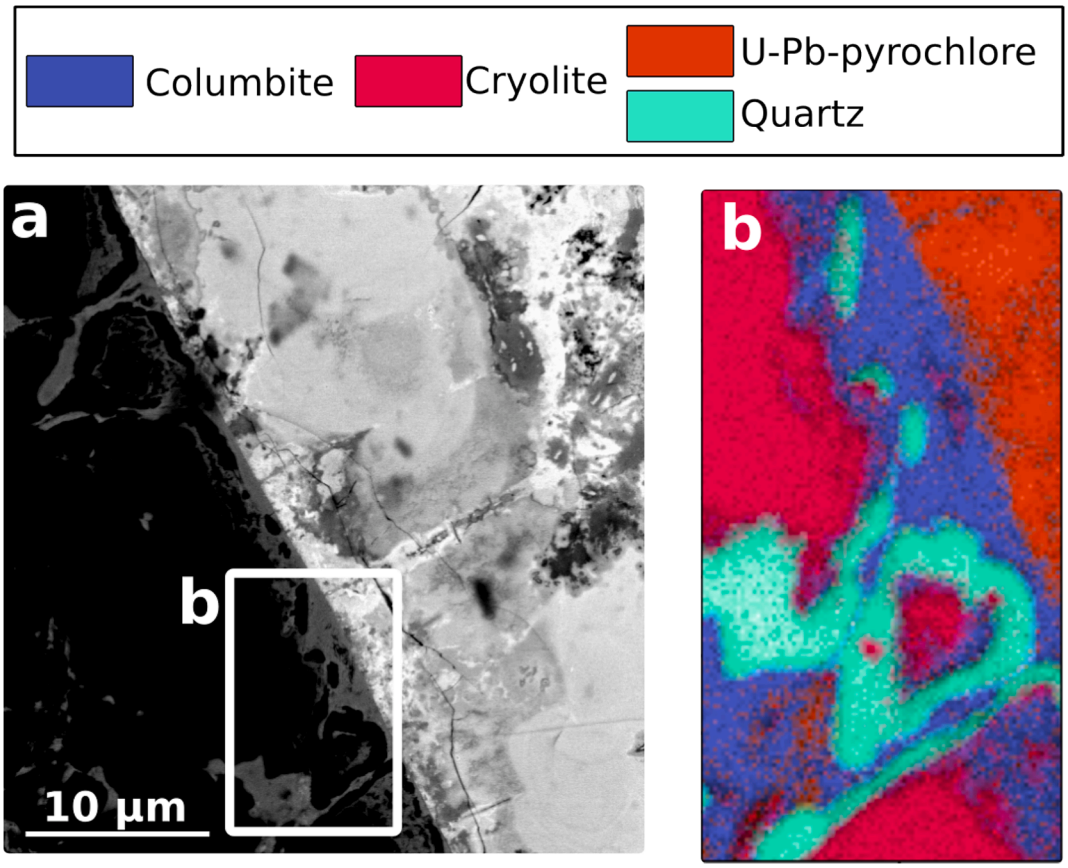

Fig. 4. (a) Backscattered electron image of the interface of an altered Pb-U-bearing pyrochlore from the CAG samples. (b) Mineral map of a Pb-U-bearing pyrochlore border at the micrometric-scale. Four phases (columbite, cryolite, quartz and Pb-U-bearing pyrochlore) have been identified using multivariate statistical analysis.

Table 2
EPMA data of pyrochlores from the CAG and BAG samples. Names are based on the two largest proportions of the A-site cations (in wt.%) for (Pcl.1) Y-U bearing pyrochlore, (Pcl.2) Y-Pb-bearing pyrochlore, (Pcl.3) Y-U-bearing pyrochlore, (Pcl.4) Pb-U-bearing pyrochlore, (Pcl.5) Y-U-bearing pyrochlore, (Pcl.6) Y-Mn-bearing pyrochlore. The high concentration of Sn in Pcl.5 is due to the inclusions of cassiterite.

wt%	Pcl.1	Pcl.2	Pcl.3	Pcl.4	Pcl.5	Pcl.6
A-site						
CaO	0.32	0.26	0.23	0.24	0.30	0.35
MnO	0.23	0.09	0.05	0.03	1.06	3.35
Na_2O	0.05	0.00	< b.d.	< b.d.	0.06	0.04
PbO	1.16	6.17	4.89	7.32	0.43	0.54
SnO	0.16	0.14	0.10	0.13	17.17	0.38
ThO_2	2.16	1.51	1.35	1.39	0.81	1.39
UO_2	3.59	4.78	6.86	6.75	3.27	2.23
ZrO_2	< b.d.	< b.d.	0.03	0.01	0.07	< b.d.
Y_2O_3	11.55	7.61	6.69	6.63	8.00	8.70
La_2O_3	0.01	0.11	0.08	0.03	0.04	0.03
CeO_2	0.45	0.69	1.01	0.97	0.31	0.46
Nd_2O_3	0.32	0.35	0.31	0.34	0.32	0.33
Sm_2O_3	0.16	0.13	0.13	0.14	0.11	0.16
B-site						
Al_2O_3	0.55	0.79	1.00	0.97	0.38	0.41
Fe_2O_3	1.77	1.50	1.27	1.27	1.32	4.43
Nb_2O_5	36.41	34.59	33.91	33.02	34.42	48.52
Ta_2O_5	5.79	5.66	8.29	8.57	5.30	8.66
TiO_2	1.88	1.06	0.86	0.76	2.90	2.28
SiO_2	6.85	8.32	9.61	10.23	6.87	1.56
F	0.79	0.79	0.57	0.55	1.41	1.00
$F = O_2$	−0.33	−0.33	−0.24	−0.23	−0.59	−0.42
Total	73.06	73.43	76.43	78.57	82.56	83.39
Normalization to 2B-site cations						
A-site						
Ca	0.02	0.02	0.02	0.02	0.02	0.02
Mn	0.01	0.01	0.00	0.00	0.06	0.18
Na	0.01	0.00	< b.d.	< b.d.	0.01	0.01
Pb	0.02	0.12	0.09	0.13	0.01	0.01
Sn	0.01	0.00	0.00	0.00	0.55	0.01
Th	0.03	0.02	0.02	0.02	0.01	0.02
U	0.06	0.07	0.10	0.10	0.05	0.03
Zr	< b.d.	< b.d.	0.00	0.00	0.00	< b.d.
Y	0.43	0.28	0.24	0.23	0.31	0.29
La	0.00	0.00	0.00	0.00	0.00	0.00
Ce	0.01	0.02	0.02	0.02	0.01	0.01
Nd	0.01	0.01	0.01	0.01	0.01	0.01
Sm	0.00	0.00	0.00	0.00	0.00	0.00
Total A-site	0.62	0.56	0.51	0.54	1.06	0.59
B-site						
Al	0.05	0.07	0.08	0.08	0.03	0.03
Fe	0.10	0.09	0.07	0.07	0.08	0.23
Nb	1.16	1.10	1.02	0.99	1.13	1.38
Ta	0.11	0.11	0.15	0.15	0.10	0.15
Ti	0.10	0.06	0.04	0.04	0.16	0.11
Si	0.48	0.58	0.64	0.68	0.50	0.10

Supérieure des Mines de Paris (MINES ParisTech) collection. Niobium-bearing hematite was prepared using the hydrothermal synthesis described in Bollaert et al., 2023c.

The average Nb speciation was quantitatively determined by performing a least-squares linear combination fit (LS-LCF) using Larch package (Newville, 2013). In this procedure, the spectra of the CAG and BAG samples were fitted with the spectra of the mineral references. The relative proportion of each component indicates the contribution of each mineral to the average Nb speciation within the granites. The sum of the contributions was set to 1.

3. Results

3.1. Characterization of the niobium mineralization at the micron scale

3.1.1. Textures and compositions of pyrochlores

Microscopic observations indicate that pyrochlore is the main Nb mineral in the Madeira albite-enriched granites (Fig. 2). In the CAG sample, pyrochlore is chemically characterized by high concentrations of Pb and U (Fig. 3a,b). Pyrochlores form large crystals of several hundreds of micrometers and are overgrown by cryolite (Fig. 2a,c). All investigated pyrochlores display corrosion features (Fig. 2a,c). A close-up on the pyrochlores from CAG sample indicates chemical heterogeneity at the micrometric scale (Fig. 4a). The mineral map retrieved on a corroded zone of a U-Pb-pyrochlore from the CAG sample shows that columbite is formed at the contact of pyrochlore as a rim of a few micrometers (Fig. 4b). Quartz and cryolite are also associated with columbite (Fig. 4b). Other phases have been identified in the heterogenous corroded zones of pyrochlores such as bastnaesite (Fig. 2d), micro-inclusions of cassiterite (Fig. 2b), and Nb-bearing Fe oxide veins (Fig. 2d).

In the BAG sample, pyrochlores are extensively replaced by columbite-(Mn), forming a pseudomorph-like texture (Fig. 2e). They are characterized by higher concentrations in Y than pyrochlores from the CAG sample with variable amounts of Pb and U (Fig. 3c, Table 2). A mineral map obtained for an altered pyrochlore in the BAG shows that about 30 % of pyrochlore is replaced by columbite-(Mn) (Fig. 5, Table 3). Fluorite (CaF_2) and pyrite (FeS_2) are found in the vicinity of Y-Pb rich pyrochlores (Fig. 2e, Fig. 5b). The border of fluorite is characterized by a submicrometric reaction interface rich in Y, although low thickness precludes chemical characterization using SEM-EDS (Fig. 2f). Another compositional type of pyrochlore rich in U and Pb has been evidenced (Fig. 3a). It forms smaller crystals (< 100 μm) than the Pb-U and Y-bearing pyrochlore (Fig. 2g,h). Columbite and F-bearing minerals such as cryolite and fluorite are not observed with this type of pyrochlore. Nanocrystallized U-bearing veins extend outwards U-Pb-bearing pyrochlore (Fig. 2g,h).

3.1.2. Textures and compositions of other niobium-bearing minerals

Uranium-bearing veins containing elements such as F, P, and heavy rare earth elements (HREE), in which Nb is detected as a minor element, are found in CAG sample (Fig. 6a). They appear texturally heterogeneous and nanocrystallized at smaller scale (Fig. 6b). Large crystals of Nb-Sn-bearing Fe oxide with inclusions of columbite and Nb-bearing cassiterite are found in the BAG sample (Fig. 6c,d). Iron oxides, exhibiting tabular microfacies in orthoclase also contain Nb in the BAG sample (Fig. 6e,f).

3.2. Nanometric scale investigation of niobium minerals

The micrometric size of some Nb-bearing phases prevented definitive identification with SEM-EDS. Chemical and mineralogical analyzes of Nb-bearing veins and reaction interfaces were thus performed using TEM on three FIB sections: (1) a U-bearing vein containing Nb in CAG sample (Fig. 6a), (2) a Y-Nb-Fe-rich areas at the border of fluorite in BAG sample (Fig. 2f), (3) a mineralogical interface between columbite and pyrochlore in CAG sample (Fig. 2d).

Observed under TEM, the U-bearing vein is heterogeneous and characterized by porous zones, sometimes partially filled (Fig. 7b). STEM-EDS mapping reveals that only the porous zones concentrate Nb (Fig. 7c). Electron diffraction patterns acquired in two distinct zones of the U-bearing vein indicate that the vein is composed of two minerals (Fig. 7d). The diffraction pattern repetition of the Nb-poor regions of the vein indicates a monocrystalline phase, displaying diffraction spots corresponding to interplanar distances of 2.78, 1.83, 1.61, 1.45 Å, characteristic of the (211), (312), (411), (332) planes of coffinite (Fuchs and Gebert, 1958) with the formula $U(SiO_4)_{1x}(OH)_{4x}$ (Fig. 7e). The

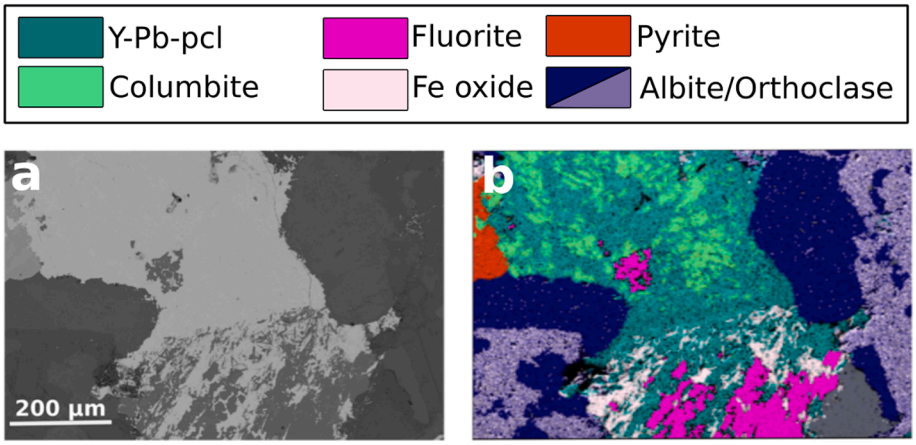

Fig. 5. (a) Backscattered electron image of a Y-Pb-bearing pyrochlore from the BAG sample. (b) Mineral map evidencing the presence of columbite areas in pyrochlore as revealed by multivariate statistical analyses. Fluorite, Fe oxide, pyrite, albite and orthoclase are also identified.

Table 3
EPMA data of columbite-(Mn) found in the BAG facies.

wt%	Col.1	Col.2	Col.3	Col.4	Col.5
A-site					
CaO	0.06	0.10	0.02	0.06	0.09
MnO	10.14	10.01	12.97	6.17	14.85
FeO	6.48	6.11	6.14	5.07	2.42
Na_2O	0.02	0.02	0.01	0.01	0.02
PbO	< b.d.	< b.d.	< b.d.	0.94	< b.d.
SnO	0.13	0.32	0.34	0.43	0.78
ThO_2	0.03	0.27	0.20	0.61	0.39
UO_2	0.00	0.40	0.02	1.82	0.14
ZrO_2	0.03	0.01	0.00	0.00	0.02
Y_2O_3	0.02	1.68	0.08	5.10	0.20
La_2O_3	0.00	0.00	0.01	0.05	< b.d.
CeO_2	0.00	0.12	< b.d.	0.42	0.06
Nd_2O_3	0.05	0.14	< b.d.	0.12	0.01
Sm_2O_3	0.10	0.09	0.12	0.15	0.12
B-site					
Al_2O_3	0.06	0.16	0.00	0.16	0.00
Nb_2O_5	66.43	63.63	68.12	67.89	69.16
Ta_2O_5	7.53	8.69	6.61	6.65	8.37
TiO_2	1.17	1.28	0.69	0.76	0.53
SiO_2	< b.d.	< b.d.	< b.d.	< b.d.	< b.d.
Total	92.26	93.06	95.31	96.43	97.16
Normalization to 6O atoms					
A-site					
Ca	0.00	0.01	0.00	0.00	0.01
Mn	0.54	0.53	0.67	0.32	0.75
Fe	0.34	0.32	0.31	0.26	0.12
Na	0.00	0.00	0.00	0.00	0.00
Pb	0.00	0.00	0.00	0.02	0.00
Sn	0.00	0.01	0.01	0.01	0.02
Th	0.00	0.00	0.00	0.01	0.01
U	0.00	0.01	0.00	0.03	0.00
Zr	0.00	0.00	0.00	0.00	0.00
Y	0.00	0.06	0.00	0.17	0.01
La	0.00	0.00	0.00	0.00	0.00
Ce	0.00	0.00	0.00	0.01	0.00
Nd	0.00	0.00	0.00	0.00	0.00
Sm	0.00	0.00	0.00	0.00	0.00
Total A-site	0.89	0.94	1.00	0.83	0.92
B-site					
Al	0.00	0.01	0.00	0.01	0.00
Nb	1.87	1.80	1.87	1.87	1.87
Ta	0.13	0.15	0.11	0.11	0.14
Ti	0.06	0.06	0.03	0.04	0.02
Si	0.00	0.00	0.00	0.00	0.00

polycrystalline diffraction pattern of the Nb-rich zone (Fig. 7f) has interplanar distances of 3.21, 2.72, and 1.97 Å, characteristic of the (111), (200), and (220) planes of uraninite (3.16, 2.73, and 1.93 Å, respectively) (Wyckoff, 1963). The major elements in the vein are U and Si with minor F, Na, P, and Nb (Fig. 7g,h). The main difference between the two EDS spectra is the visible Nb signal in the porous uraninite zone (Fig. 7h). The significant Si signal in uraninite region may arise from the vicinity of coffinite (Fig. 7h).

The fluorite border is characterized by a porous and finely-crystallized phases rich in Y, Nb, and Fe (Fig. 8a,b). These phases consist in hematite and a heterogeneous zone as observed by STEM-HAADF (Fig. 8c). The latter is a mixture of nanoscale Nb-rich veins with areas richer in Y and less concentrated in Nb (Fig. 8d,e). The Y-rich region (Fig. 8e) is also characterized by the presence of F, Al, Si, Ca, and REE (Ce, Nd, Sm, Gd, Dy, Er, Yb) (Fig. 8i). The diffraction pattern of this phase highlights interplanar distances of 3.74, 3.51, 2.25, 1.89 Å, corresponding to the (011), (020), (220), and (301) planes obtained in waimirite-(Y) with the formula (Y,REE)F_3 (Atencio et al., 2015). In the nanoscale veins (Fig. 8d), Nb is the major element with significant concentrations of Y, Si, Fe, U, and HREE (Dy, Er, Yb) (Fig. 8h). The electron diffraction-derived interplanar distances are 3.17, 2.79, 2.46 Å, corresponding to the $(1\bar{2}1)$, (040), (002) planes of fergusonite-(Y) ($YNbO_4$) (Guastoni et al., 2010), which is consistent with the STEM-EDS spectrum (Fig. 8h).

Micrometric investigation of CAG sample evidences the mineralogical complexities of the ore phases with the association of monazite, cassiterite, columbite and pyrochlore over a 10 μm^2 area (Fig. 2d). Despite the presence of Nb in both pyrochlore and columbite, there are higher amounts of Nb in the Fe-rich zones, corresponding to columbite (Fig. 9c,d). Columbite also forms nanometric veins within pyrochlore (Fig. 9d). Uranium and Pb hot spots are found at the interface between pyrochlore and columbite (Fig. 9d).

3.3. Atomic-scale characterization of niobium minerals by Nb L_3-edge XANES

The Nb L_3-edge XANES spectra were collected in columbite, Pb-U-bearing, pyrochlore, Nb-bearing hematite, Nb-bearing uraninite, and Nb-bearing cassiterite. The latter were compared with the spectra of our reference set (Fig. 10). All spectra exhibit a white line with two maxima, namely, A and B (Fig. 10). The position and width of the B features are particularly sensitive to the atomic environment of Nb (Bollaert et al., 2023c), making them useful for distinguishing between different Nb hosts.

The XANES spectra obtained from pyrochlore and columbite crystals, located tens of micrometers apart, display distinct spectral profile (Fig. 10a) which match with those of the corresponding references. Features B of Pb-U-bearing pyrochlore and columbite are centered at 2376.2 eV and 2375.9 eV, respectively. The Nb-bearing Fe oxide XANES

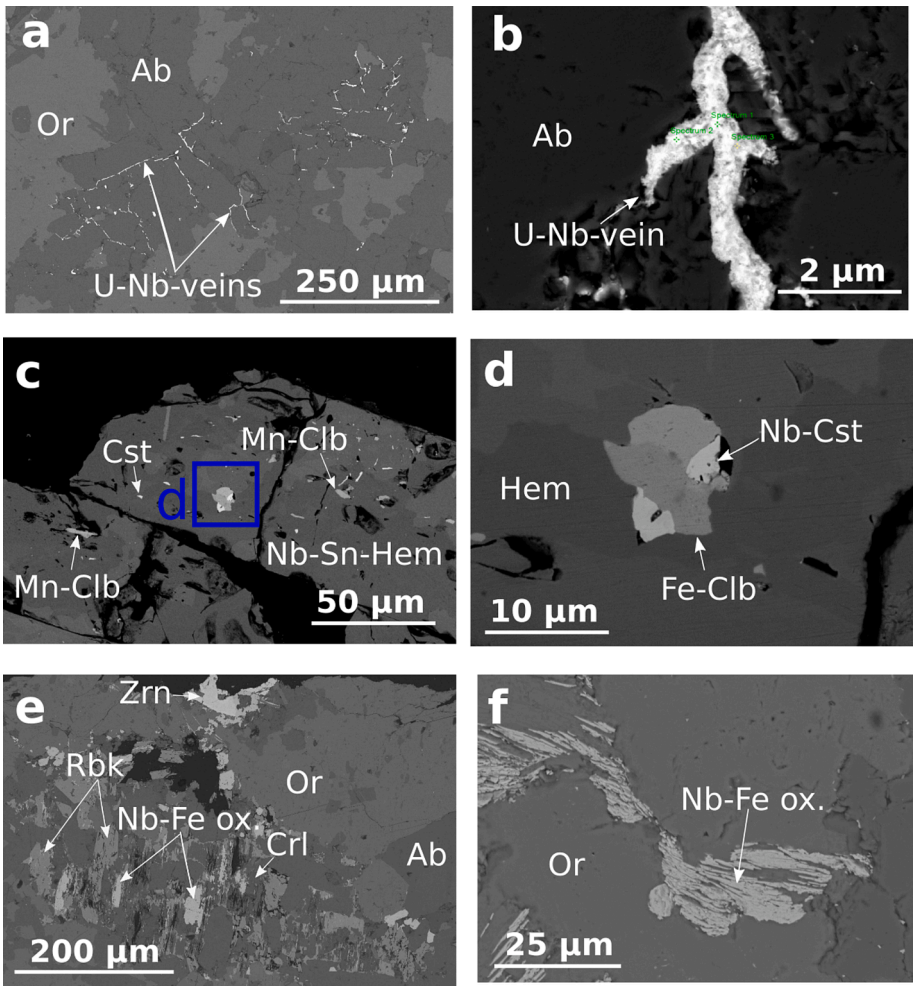

Fig. 6. (a) Micrometric U-Nb-rich veins crosscutting albite (Ab) in the CAG sample. (b) Nanocrystallized U-Nb-rich vein in the BAG. (c) Large tabular crystals of Nb-bearing Fe oxide with inclusions of columbite-(Mn) (Clb-Mn) and cassiterite (Cst). (d) Close-up on a columbite-(Fe) (Clb-Fe) crystal intertwined with Nb-bearing cassiterite (Nb-Cst) visible in (c). (e) Crystals of cryolite (Crl) and Nb-bearing Fe oxides formed at the expense of riebeckite (Rbk). (f) Micrometric-sized crystals of tabular Nb-bearing Fe oxide in orthoclase (Or).

spectrum exhibits narrow B features with similar intensities located at 2375.8 eV, resembling that of Nb-bearing hematite (Fig. 10b). The XANES spectrum of Nb-bearing uraninite stands out due to the smaller magnitude between the A and B features at the positions of 2372.7 and 2375.4 eV, respectively. In absence of reference spectrum for uraninite, the only XANES spectrum with such low magnitude between the A and B features is that of U-bearing oxynatropyrochlore (Fig. 10c). Differences in feature widths and relative intensities are though noted (Fig. 10c). Finally, the XANES spectrum of Nb-bearing cassiterite is characterized by an additional shoulder at 2378.5 eV (Fig. 10d), absent from the reference spectra.

3.4. Average niobium speciation

A least-squares linear combination fitting (LS-LCF) procedure of Nb L_3-edge XANES spectra on the granite bulk samples was performed. The spectra used as fitting components were selected based on the finger-print analysis (Fig. 10), and spatially-resolved chemical analyses using SEM. Given the scarcity of Nb-bearing hematite and the low amounts of Nb in the albite-enriched granites, this spectrum was not taken into account in the fitting procedure. In the absence of visible shoulder at ca. 2378.0 eV (Fig. 10d), the spectrum of Sn-Nb-bearing mineral was neither considered as a fitting component. The fit with hydropyrochlore and columbite spectra fails to accurately reproduce the bulk spectra of the BAG and CAG samples (Fig. S3). The only reference spectrum that significantly improves the fit and is abundantly observed in SEM-EDS analyses is U-bearing oxynatropyrochlore. The best fit of the CAG spectrum is obtained with 53 % U-bearing oxynatropyrochlore, 37 % hydropyrochlore and 10 % columbite (Fig. 11a). The BAG spectrum is fitted with 63 % U-bearing oxynatropyrochlore, 33 % columbite and 3 % hydropyrochlore (Fig. 11b).

4. Discussion

4.1. Alteration of pyrochlore by columbite (columbitization)

The systematic presence of overgrowths and pseudomorphs of columbite around pyrochlore (Fig. 2a,b,c,d,e) is consistent with the hydrothermal origin of columbite (Minuzzi et al., 2005; Bastos Neto et al., 2009; Hadlich, 2023). The formation of columbite results from the replacement of the A-site cations of pyrochlore by Fe^{2+} (and/or Mn^{2+}) and the leaching of Y-sites of the pyrochlore structure (Nasraoui and Bilal, 2000; Chakhmouradian et al., 2015; Tremblay et al., 2017), in the form of:

$$H^{+}_{(aq)} + Fe^{2+}_{(aq)} + (CaNaNb_2O_6F)_{(s)} = FeNb_2O_{6(s)} + Ca^{2+}_{(aq)} + Na^{+}_{(aq)} + HF_{(aq)} \quad (1)$$

This process of conversion of pyrochlore into columbite suggests a solid-state transformation if ion exchanges only are involved. However, the

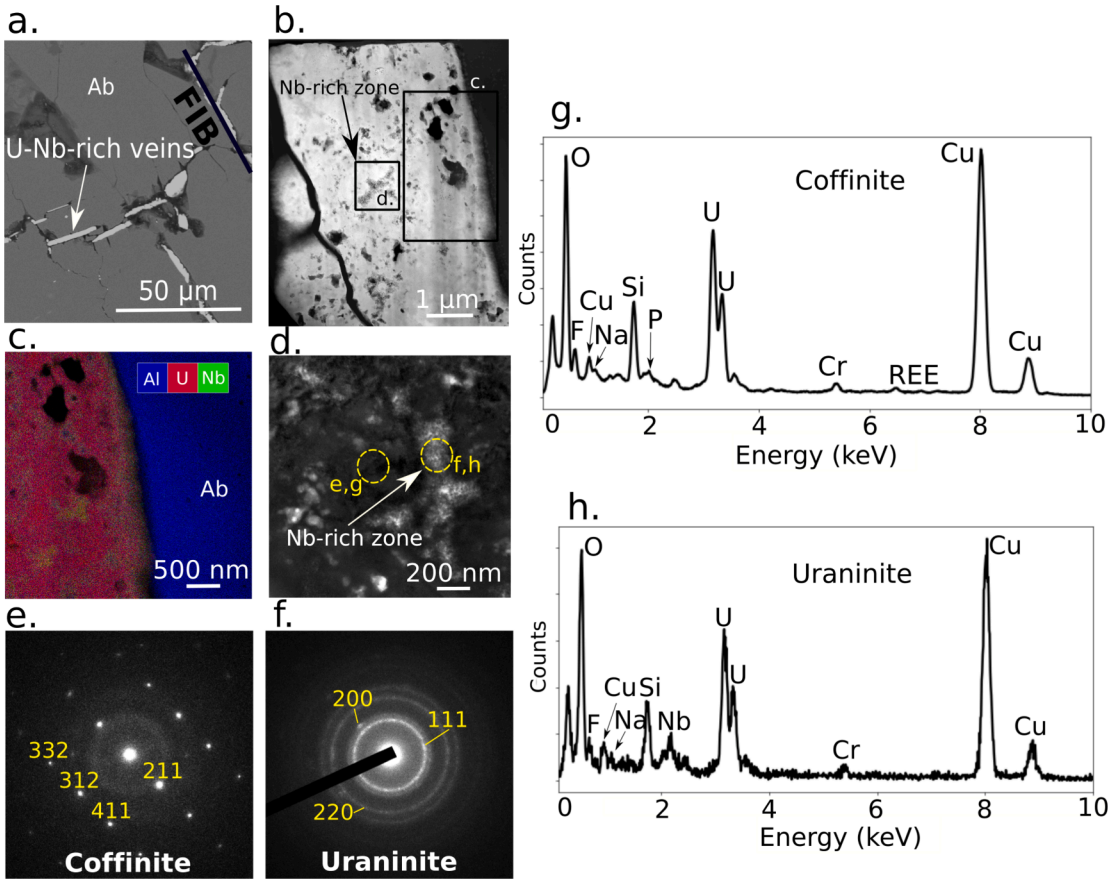

Fig. 7. Nanoscale characterization of U-bearing Nb-bearing veins in the CAG sample. (a) Backscattered electron SEM images of U-bearing veins traversing albite (Ab). The black line indicates the location of FIB section. (b) HAADF image of the FIB section. (c) STEM-EDS RGB map of the interface between the vein and albite highlighting Nb-rich porous areas. (d) TEM image of the area marked in (b). (e-f) Electron diffraction patterns characteristic of coffinite and uraninite, respectively. (g-h) STEM-EDS spectra acquired from the area indicated in (d) Nb-depleted coffinite and Nb-bearing uraninite, respectively.

distinct spectral features of the Nb L_3-edge XANES spectra indicate that the atomic-scale environment of Nb in columbite and pyrochlore are distinct (Fig. 10a). These differences reflect the expected stronger distortion of edge-sharing Nb octahedra in columbite compared to corner-sharing Nb octahedra in pyrochlore (Bollaert et al., 2024). Such major structural changes occurring during the columbitization process, which are unlikely achieved by ion exchanges, involve a dissolution-reprecipitation mechanism leading to the complete alteration of pyrochlore. This mechanism contradicts the expected resistance of pyrochlore to alteration (Lumpkin and Ewing, 1995; Wall et al., 1996; Cordeiro et al., 2011; Smith and Spratt, 2012; Zaitsev et al., 2011; Walter et al., 2018; Dey et al., 2021, Hadlich, 2023). The nanometric zones enriched in U and Pb at the interface between pyrochlore and columbite (Fig. 9) may also result from the dissolution processes leading to their release to the fluids and their subsequent immobilization. This dissolution-reprecipitation mechanism is corroborated by the analysis of experimentally altered pyrochlore at 100–300 °C (Xu et al., 2004; Pöml et al., 2007). In contrast to this study, columbite has not precipitated in their experiments due to the absence of Fe and Mn ions in the leach solutions whereas the precipitation of columbite is expected to be stable in fluids with high Fe activities and low Ca and Na activities (Lumpkin and Ewing, 1995).

Columbitization and hydrothermal alteration of pyrochlore into Nb-bearing Ti oxides have been commonly described in carbonatites (Verwoerd et al., 1995, Melgarejo et al., 2012, Chebotarev et al., 2017; Wu et al., 2021). However, the columbitization observed in the Madeira granite represents the only documented occurrence of such alteration in granitic systems.

4.2. *Influence of the crystal-chemistry of pyrochlore on the formation of secondary minerals*

In both CAG and BAG samples, we evidenced the presence of diverse nanometric phases associated with pyrochlore (Figs. 7 and 8). In the BAG sample, the similar crystal-chemistry of the Nb-REE-bearing nanometric phases, and their association with Y-Pb-bearing pyrochlore (Fig. 8a,b) indicates their parental relationship. The absence of secondary pyrochlore resulting from the alteration of Y-Pb-bearing pyrochlore is likely due to the mobilization of soluble Pb^{2+}, not providing enough A-site cations to precipitate pyrochlore, and the low temperature of alteration. Instead, waimirite-(Y) and fergusonite-(Y) have precipitated due to the release of Nb and REE from Y-Pb-bearing pyrochlore (Fig. 8). Waimirite-(Y) is a rare fluoride mineral, only described in hydrothermal veins from the Madeira albite-enriched granites and in the hydrothermally altered microgranite at Jabal Tawlah (Atencio et al., 2015). Comparison of the STEM-EDS spectrum (Fig. 8i) with the reference composition of waimirite-(Y) (Atencio et al., 2015) suggests that waimirite-(Y) likely does not contain Nb. The Nb signal instead likely originates from the presence of fergusonite-(Y) in the nearby nanometric region (Fig. 8d,e). The conditions of formation of waimirite-(Y) are not well documented. In the BAG sample, the precipitation of waimirite-(Y) may have occurred just after the leaching of REE from Y-Pb-bearing pyrochlore due to role of F as a depositional ligand with respect to REE (Migdisov et al., 2016). Nano-sized veins of fergusonite-(Y) may have precipitated after the formation of waimirite-(Y) with the remaining Nb^{5+} from Y-Pb-bearing pyrochlore that could not incorporate the structure of waimirite-(Y). Fergusonite-(Y) is considered as one of the

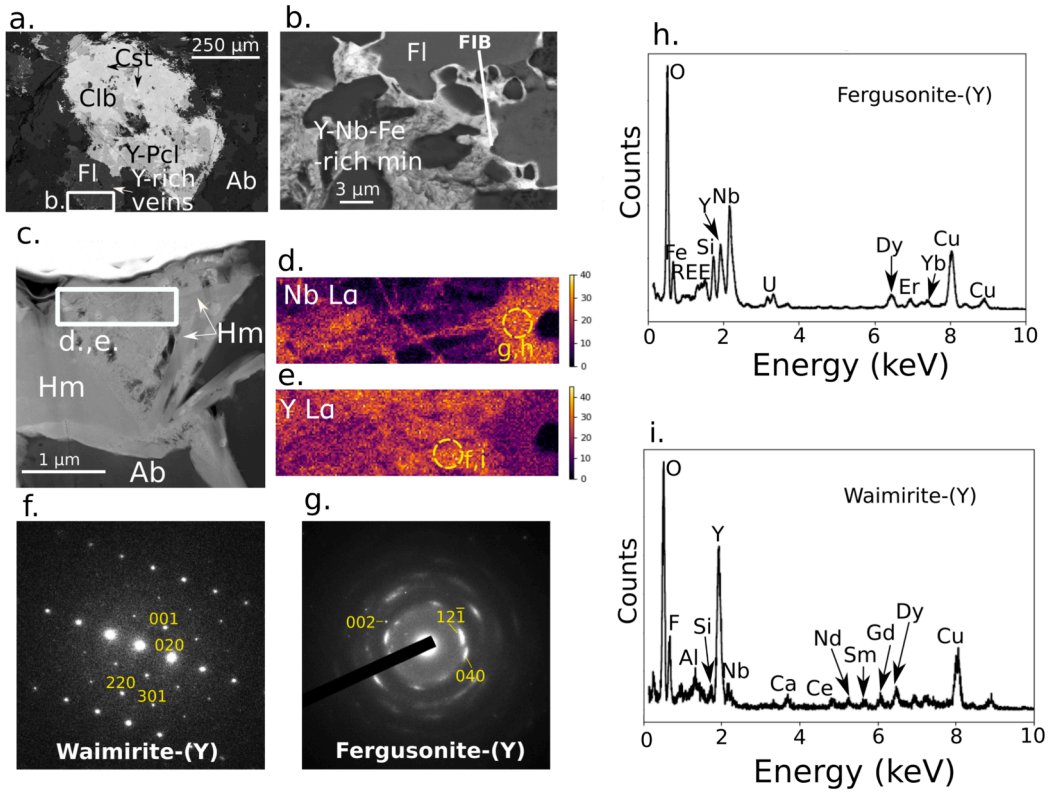

Fig. 8. Nanoscale characterization of Y-Nb-rich fluorite rim in the BAG sample. (a-b) Backscattered electrons SEM image of veins and fluorite (Fl) rim rich in Y, Nb, and Fe and a pyrochlore (Pcl) partially replaced by cassiterite (Cst) and columbite (Clb). The white rectangle corresponds to a close-up on the fluorite rim exhibiting a porous texture (b). The white line indicates the location of the extraction of the FIB section. (c) HAADF image of the FIB section. (d-e) STEM-EDS maps of Nb and Y focusing on the white rectangle shown in (c). (f-g) Electron diffraction pattern matching with the structure of waimirite-(Y) and fergusonite-(Y), respectively. (h-i) STEM-EDS spectra of fergusonite-(Y) and waimirite-(Y), respectively.

main Nb ore mineral in alkali granites (Ercit, 2005) and carbonatites (Ying et al., 2023). It is mainly found as a late magmatic to post-magmatic stage mineral, which can form at the expense of a precursor such as pyrochlore in the Keivey alkali granite (Zozulya et al., 2020), and eudialyte in the Strange Lake peralkaline granite (Sheard et al., 2012).

Since Pb-U-bearing pyrochlore is the only important source of U and Nb in the CAG sample (Fig. 2a-d), the formation of the micrometric U-Nb-bearing veins (Fig. 2g, 6a) likely resulted from the alteration of Pb-U-bearing pyrochlore. Coffinite was the first phase to precipitate under Si-rich, low temperature and low oxygen fugacity (typically, $f(O_2) = 10^{-69}$ atm) (Szenknect et al., 2016; Macmillan et al., 2017). The texture of uraninite characterized by polycrystalline nanodomains in porous zones of coffinite, suggests that it may have subsequently formed from coffinite. Although the formation of coffinite from uraninite is common and has been well-studied (Szenknect et al., 2020), the opposite transformation exists but has been much less documented (Janeczek and Ewing, 1992). Such phase transformation has been ascribed to amorphous coffinite upon thermal annealing at a temperature above 573 K (Lian et al., 2009). The nanocrystals of uraninite may stem from the decomposition of amorphous coffinite nanodomains as temperature rises during a second hydrothermal event. Additionally, the presence of Nb in the U-bearing vein (Fig. 7g,h) may lead to the transformation of coffinite into uraninite. The incorporation of Nb^{5+} in coffinite can be described by the following substitution mechanism: $REE^{3+} + Nb^{5+} = U^{4+} + Si^{4+}$ (Macmillan et al., 2017). Considering the expected high levels of Nb in fluids resulting from pyrochlore alteration, the subsequent removal of Si from coffinite might have prompted the formation of Nb-Si-bearing uraninite, a host already described for Nb (Frimmel et al., 2014; Wu et al., 2021; Wertich et al., 2022). While Nb-bearing uraninite has also been observed in the Miaoya carbonatite (Wu et al., 2021), the absence of coffinite in this geological context is attributed to the low Si content.

The similarity in composition of pyrochlore and its secondary products suggests that the composition of Madeira pyrochlore controls the nature of the resulting alteration phases. This phenomenon, wherein the crystal chemistry governs the formation of alteration phases, has also been observed in other systems. For instance, Nb-bearing uraninite and Nb-bearing rutile have been identified after the alteration of Ti-bearing uranpyrochlore (Wu et al., 2021), betafite ($A_2Ti_2O_6(OH)$) has been observed after Ti-bearing pyrochlore (Deditius et al., 2015), and aeschynite has been found after REE-bearing betafite (Pöml et al., 2007). However, this dependence on crystal chemistry has not been observed in supergene environments, where the alteration of any composition of pyrochlore yields Nb-bearing goethite due to the high concentration and insolubility of Fe^{3+}, which precipitates locally and incorporates Nb (Wall et al., 1996; Melgarejo et al., 2012; Chebotarev et al., 2017; Bollaert et al., 2023a,b).

4.3. *Effect of the hydrothermal processes on the average niobium speciation and ore grade*

Although this study highlights various Nb mineralogical hosts (Pb-U-bearing pyrochlore, U-Pb-bearing pyrochlore, Y-bearing pyrochlore, columbite, Nb-bearing hematite, Nb-bearing cassiterite, fergusonite-(Y), and Nb-bearing uraninite), only pyrochlores and columbite significantly contribute to the average Nb speciation (Fig. 11). This is consistent with the high amounts of pyrochlore and their high Nb concentrations (Table 2 and Table 3), while the other carriers are scarce and with less Nb. Two types of pyrochlore reference spectra were used in the fitting procedure to account for the variety of the pyrochlore composition found in the albite-enriched granites (Fig. 3). The XANES spectrum of U-

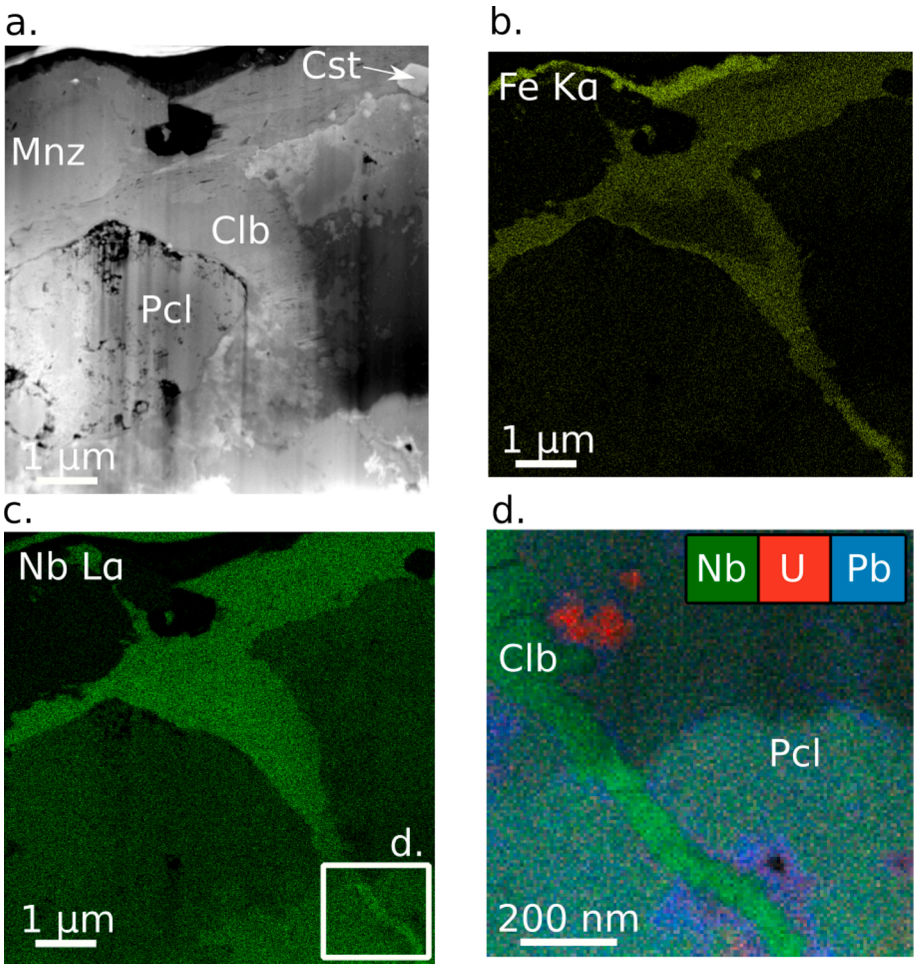

Fig. 9. Nanoscale characterization on a mineralogical interface between pyrochlore and columbite located in Fig. 2d. (a) HAADF image of the FIB section. (b-c) STEM-EDS maps of Fe and Nb, respectively. (d) STEM-EDS RGB map of the area delimited by a white square in (c).

bearing oxynatropyrochlore of reference is used to represent the Madeira U-bearing pyrochlore in the fitting procedure (Fig. 10c). The resemblance between the U-bearing oxynatropyrochlore and Nb-bearing uraninite spectra (Fig. 10c) suggests that some minor proportion of the U-bearing oxynatropyrochlore contribution may correspond to that of Nb-bearing uraninite. These similarities arise from their poor crystallinity, leading to increased structural disorder and longer Nb–O distances compared to other non-metamict references. The hydropyrochlore XANES spectrum is used to account both Pb-U-bearing and Y-bearing pyrochlores. Given the similarities between XANES spectra of crystalline pyrochlore (Bollaert et al., 2023c) and the quality of the BAG and CAG spectra fitting, the hydropyrochlore reference spectrum can be used to encompass both Pb-U-bearing and Y-bearing pyrochlore spectra.

Using previous studies on the genesis of Nb mineralization at Madeira, U-Pb-bearing pyrochlore is considered to have a magmatic origin (Bastos Neto et al., 2009; Hadlich, 2023). In contrast, the formation of Pb-U-bearing and Y-bearing pyrochlores represents an early stage of hydrothermal alteration, while the formation of columbite at the expense of pyrochlore reflects a phase of intense hydrothermal alteration. The LS-LCF analysis indicates that approximately 10 % and 33 % of the magmatic pyrochlores in the CAG and BAG samples, respectively, have undergone columbitization (Fig. 11). The detection of pyrochlore on XRD pattern of the CAG sample but absent from the BAG sample (Fig S1 and Fig S2) also aligns with the higher degree of columbitization of pyrochlore in the BAG sample. The latter also exhibits the highest Nb concentration, at 1597 ppm. Comparing the quantitative average Nb speciation with bulk concentrations suggests that hydrothermal processes have increased the Nb ore grade of the Madeira albite-enriched granites. This enhancement is mainly due to the columbitization process (Bastos Neto et al., 2009), resulting from the higher relative enrichment of Nb in columbite compared to pyrochlore (Tables 2 and 3). Similar increases in Nb ore grade due to hydrothermal processes have been observed in the Nb-Ta-rich granitic deposit of Lingshan (Xiang et al., 2017), the Nb-rich Tianbao trachytic complex (Yan et al., 2022) and the Shuanghekou Nb trachytic deposit (Wu et al., 2023). In contrast, the hydrothermal alteration of the REE-Nb-rich carbonatitic complex of Miaoya (Wu et al., 2021; Ying et al., 2023) and the Nb-Ta-W-Sn-rich granite of Zhaojinggou (Zhang et al., 2023), has not led to an the increase in the ore grade.

4.4. *Evidence and conditions of niobium mobilization*

In the CAG sample, the micrometric Nb-bearing U minerals in feldspars in the absence of pyrochlore vicinity (Fig. 6a,b) shows that Nb and U mobility range may exceed the mineralogical scale. Investigation of the nanometric Nb-bearing minerals provides insights on the physical–chemical features of the hydrothermal alteration elucidating the mobility of these elements. The presence of F in Nb-bearing uraninite and coffinite (Fig. 7g,h) evidences the extensive co-transport of Nb and U in a F-rich hydrothermal fluid. The maximum concentration of Nb carried by the fluids can be estimated from the Nb concentration in uraninite (ca. 1 wt% Nb according to SEM-EDS analyses). This solubility is higher than reported in the literature (ca. 90 ppm Nb, Kotova, 2012),

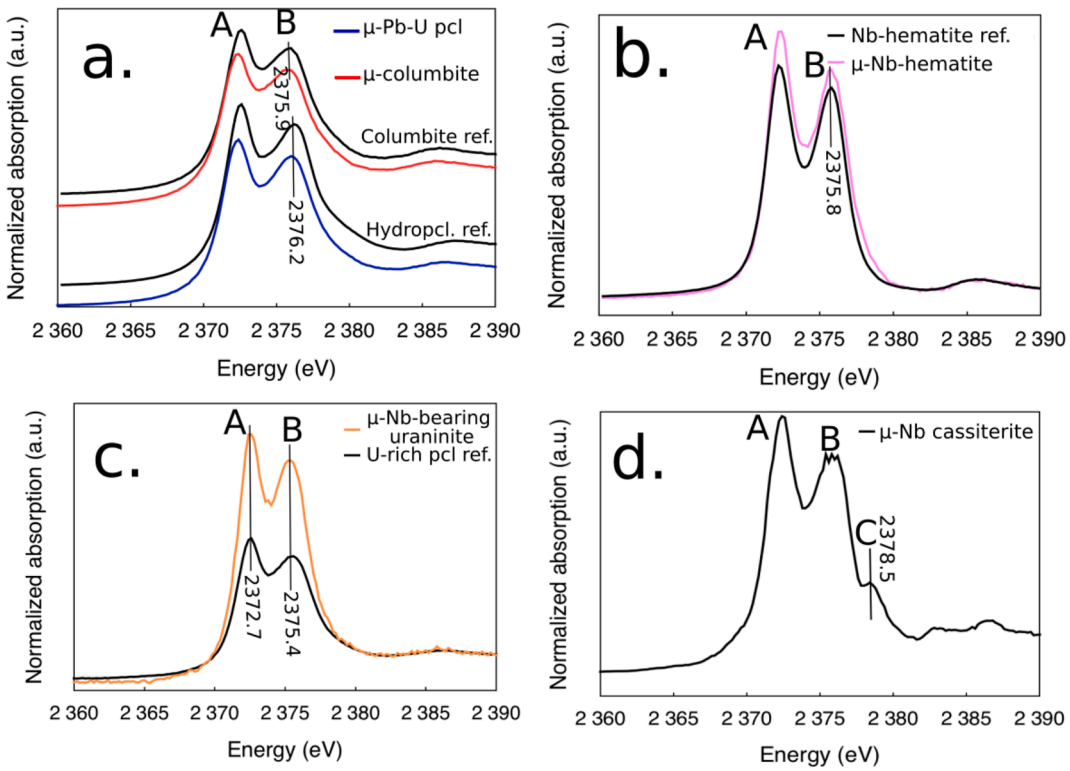

Fig. 10. Comparison of XANES spectra at the Nb L_3-edge collected on the thin sections of the CAG and BAG samples with available reference spectra. (a) XANES spectra of pyrochlores and columbite, (b) Nb-bearing hematite, (c) Nb-bearing uraninite, (d) Nb-bearing cassiterite. No reference spectra are available for Nb-bearing uraninite and Nb-bearing cassiterite.

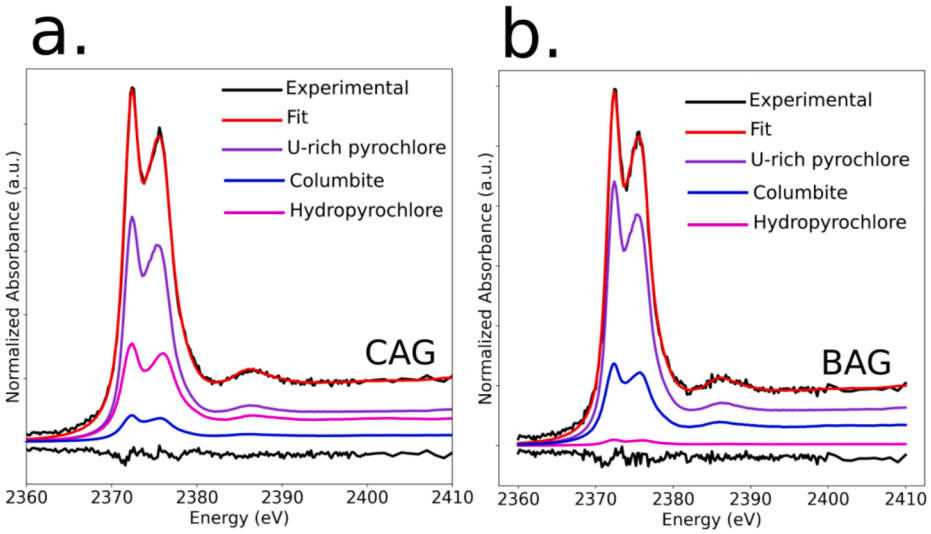

Fig. 11. Least-squares linear combination fitting (LS-LCF) procedure of the spectra from the (a) CAG and (b) BAG samples using U-bearing oxynatropyrochlore, columbite and hydropyrochlore spectra.

likely due to underestimate of F concentration. Nonetheless, the impact of Nb-F complex mobilization on the Nb ore grade was likely less important than the relative Nb enrichment resulting from the extensive columbitization process.

The nanoveins of Nb-bearing uraninite and coffinite found at Madeira differ from the ones found from the alteration of U-bearing pyrochlore in both Bayan Obo and Miaoya carbonatites which are confined to the micrometric environment of the parent mineral (Smith et al., 2018; Wu et al., 2021). The transport of U in oxidizing conditions as U^{6+} is excluded given the presence of sulphides such as pyrite, sphalerite and galena which appear to be synchronous to the columbitization event (Fig. 5). The textural features of uraninite in the carbonatites and the studied granites indicate that U^{4+} is more mobile in the presence of F ligands compared to CO_3^{2-} ligands (Peiffert and Cuney, 1996; Guillaumont and Mompean, 2003).

The nanometric association between waimirite-(Y) and fergusonite-(Y) implies a co-transport of Nb and REE in the BAG. Their formation on the fluorite border (Fig. 8a,b) and the high F concentrations in waimirite-(Y) also show the primordial role of F in their mobilization. The high concentration of F and Y, released from Y-bearing pyrochlore, in

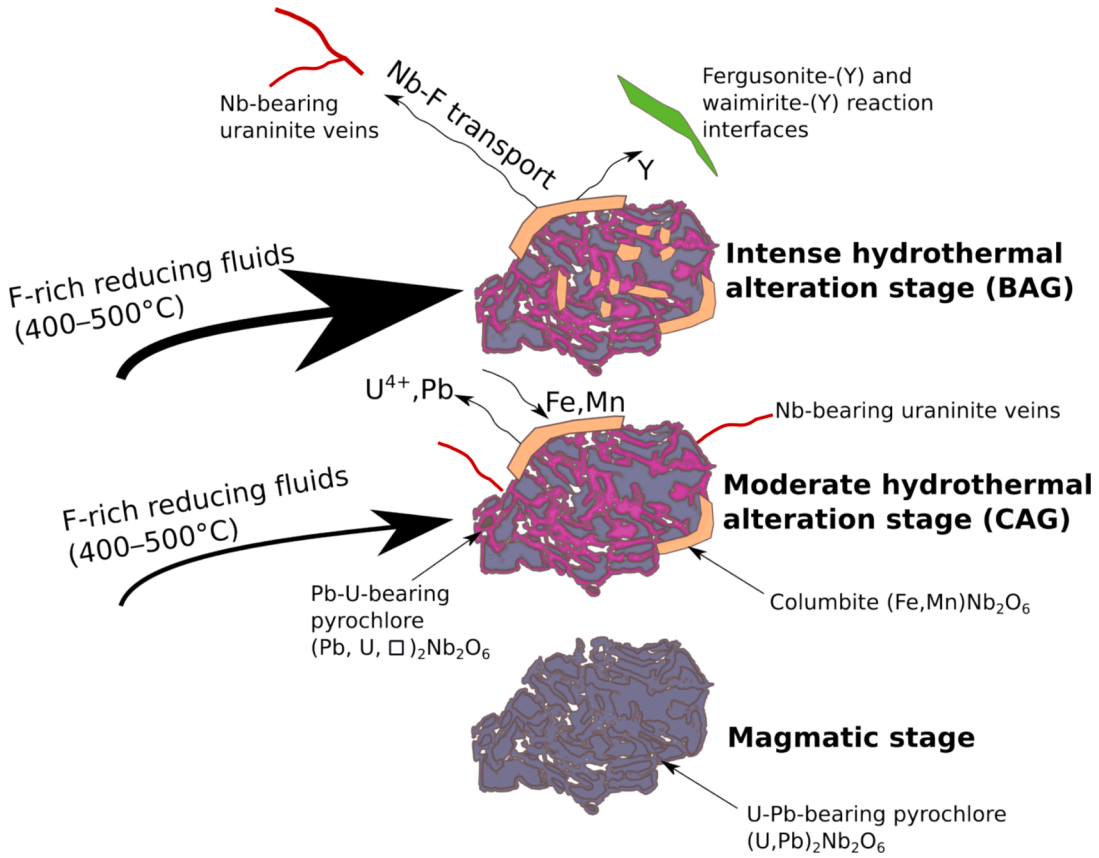

Fig. 12. Sketch showing the evolution and transport of Nb and associated elements along with alteration.

the hydrothermal fluid induced first the precipitation of waimirite-(Y) due to the depositional role of fluoride ligands with respect to REE (Migdisov et al., 2016). Due to the consumption of F by the formation of waimirite-(Y), the solubility of Nb decreases, precipitating fergusonite-(Y). The formation of waimirite-(Y) has therefore limited the mobility of Nb in the BAG. The preferential formation of fergusonite-(Y) over other $ANbO_4$ and ANb_2O_6 minerals may be indicative of an alteration temperature range of 400–500 °C (Yang et al., 2023). This is supported by observations where a combination of fergusonite-(Y) and ilmenite are locally found during the experimental hydrothermal alteration of a Nb-rich biotite at 400–500 °C, while aeschynite-(Y) and Nb-bearing rutile were formed at 600 °C (Yang et al., 2023). As the Ti concentration between the studied pyrochlores and Nb-rich biotite is of the same order of magnitude (ca. 1–3 wt% TiO_2), the Ti content alone cannot account for the absence of aeschynite and rutile formation in the studied granites. A hydrothermal temperature starting at 400 °C aligns with the homogenization temperature observed in fluid inclusions within cryolite (Bastos Neto et al., 2009). Additionally, the nature of the fluid rich in Na, which has led to the formation of cryolite, may have contributed to the precipitation of Nb-bearing oxides over Nb-rich titanates (Yang et al., 2023). The evolution of the hydrothermal Nb mineralization and transport is summarized Fig. 12.

4.5. Impact of hydrothermal alteration on niobium beneficiation

The majority of the studies conducted on Nb recovery focuses on ores from the three existing pyrochlore mining operations (Araxá, Catalão and Niobec), where the ore is subjected to reverse flotation of the gangue minerals followed by direct flotation of pyrochlore (Shikika et al., 2020). The beneficiation of columbite is also possible using a combination of magnetic and gravity concentrations, but it becomes ineffective for fine particles, resulting in Nb losses in gravity tailings (Cao et al., 2021). The flotation of columbite using selective collectors has also received increasing attention but recovery of Nb from this method remains in its early stages (Gibson et al., 2015; Shikika et al., 2020). The hydrothermal alteration of the Madeira granites, which has complexified the magmatic Nb mineralization by forming columbite closely associated to pyrochlore and new chemical varieties of pyrochlore, has downgraded the quality of the Nb ore by modifying the ore liberation including the morphological, the surficial and functional properties of the Nb ore minerals (Rajak et al., 2022). Although pyrochlore dominates the average Nb speciation of the Madeira granites, columbite is also present in substantial amount (Fig. 11). However, the current Nb recovery as Sn by-product at Pitinga fully relies on the gravity separation and flotation of pyrochlore (Bastos Neto, personal communication, 2024), involving important loss of columbite in the residue process streams. Niobium recovery could therefore be enhanced by conducting research on the mechanisms driving mineral-reagent interactions of both pyrochlore and columbite flotation systems (Gibson et al., 2015).

5. Conclusions

The Nb mineralization of the Madeira albite-enriched granites was studied using a multiscale approach combining micrometric, nanometric and atomic-scale analytical techniques. Various Nb-bearing minerals were identified including Pb-U-bearing, U-Pb-bearing, Y-bearing pyrochlore, columbite, Nb-bearing hematite, Nb-bearing cassiterite, fergusonite-(Y), and Nb-bearing uraninite. The hydrothermal alteration of primary magmatic U-Pb-bearing pyrochlore modified the composition of pyrochlore into U-Pb-bearing and Y-bearing pyrochlores, and ultimately destabilized its crystal structure. The main mineral resulting from the alteration of pyrochlore is columbite which formed following a dissolution-reprecipitation mechanism. The contribution of columbite to the average Nb speciation was determined using

Nb L_3-XANES spectroscopy, revealing that 10 % and 33 % of the primary mineralization was columbitized in the CAG and BAG samples, respectively. The Nb ore grade in the Madeira granites was increased by columbilitzation processes, which led to the relative enrichment of Nb in the minerals. Chemical analyses on the nanometric Nb minerals such as uraninite formed from the alteration of U-Pb-bearing pyrochlore yielding ca. 1 wt% Nb indicate the higher solubility of Nb in hydrothermal fluids compared to previous thermodynamic studies. Fluorides such as cryolite, fluorite and waimirite-(Y) at the micrometric and nanometric environment of the Nb-bearing minerals underscores the pivotal role of F in transporting Nb at a scale exceeding that of the mineralogical assemblage. Additionally, the presence of REE in the F-rich hydrothermal fluids are also crucial, because they precipitated as waimirite-(Y), which consumed most F available, and triggered the formation of fergusonite-(Y), thereby immobilizing Nb. Finally, the hydrothermal Nb mineralization has downgraded the quality of the Nb ore by limiting the ability to recover the entire range of Nb host phases.

Declaration of competing interest

The authors declare that they have no known competing financial interests or personal relationships that could have appeared to influence the work reported in this paper.

Acknowledgments

We acknowledge the ANR RECA (ANR-17-CE01-0012) project for providing samples for this study. Funding for part of this work was received from the TelluS-CESSUR research program of the Institut National des Sciences de l'Univers, CNRS (NanoMine). FIB experiments were supported by the French RENATECH network, the CPER Hauts de France project IMITECH and the Métropole Européenne de Lille. We thank Emmanuelle Ducloux from the University of Limoges for preparing the thin sections of the granites. We are grateful to Michel Fialin and Nicolas Rividi from the Sorbonne Université–CAMPARIS microprobe facility for their kind assistance in EPMA data acquisition. Special thanks to the late Rodney C. Ewing as well as Peter C. Burns, Ginger Sigmon, Eloïse Gaillou, and Jean-Claude Bouillard for providing reference minerals. We also thank Imène Estève and Damien Deldicque from Sorbonne University and ENS Paris, respectively, for their help with SEM analysis. Synchrotron radiation beamtime was provided by SOLEIL (proposal No. 20200969), and we thank the staff of the LUCIA beamline for their warm hospitality. This work was conducted as part of the PhD thesis of Q. Bollaert at ED398 GRNE, Sorbonne University.

Appendix A. Supplementary data

Supplementary data to this article can be found online at https://doi.org/10.1016/j.oregeorev.2024.106321.

Data availability

Data will be made available on request.

References

Akinfiev, N.N., Korzhinskaya, V.S., Kotova, N.P., Redkin, A.F., Zotov, A.V., 2020. Niobium and tantalum in hydrothermal fluids: Thermodynamic description of hydroxide and hydroxofluoride complexes. Geochim. Cosmochim. Acta 280, 102–115. https://doi.org/10.1016/j.gca.2020.04.009.

Aksyuk, A.M., 2002. Experimentally established geofluorimeters and the fluorine regime in granite-related fluids. Petrology 10, 557–569.

Atencio, D., Neto, A.C.B., Pereira, V.P., Moriyama, T., Watanabe, Y., Miyawaki, R., Coutinho, J.M.V., Andrade, M.B., Domanik, K., Chukanov, N.V., Momma, K., Hirano, H., Tsunematsu, M., 2015. Waimirite-(Y), orthorhombic YF3, a new mineral from the Pitinga mine, Presidente Figueiredo, Amazonas, Brazil and from Jabal Tawlah, Saudi Arabia: description and crystal structure. Mineral. Mag. 79, 767–780. https://doi.org/10.1180/minmag.2015.079.3.18.

Bastos Neto, A.C., Pereira, V.P., Ronchi, L.H., de Lima, E.F., Frantz, J.C., 2009. The world-class Sn, Nb, Ta, F (Y, REE, Li) deposit and the massive cryolite associated with the albite-enriched facies of the madeira A-type granite, Pitinga Mining District, Amazonas state, Brazil. Can. Mineral. 47, 1329–1357. https://doi.org/10.3749/canmin.47.6.1329.

Bollaert, Q., Chassé, M., Allard, T., Courtin, A., Galoisy, L., Landrot, G., Quantin, C., Vantelon, D., Calas, G., 2023a. Multiscale processes controlling niobium mobility during supergene weathering. Geochim. Cosmochim. Acta 353, 142–157. https://doi.org/10.1016/j.gca.2023.05.023.

Bollaert, Q., Chassé, M., Bastos Neto, A., Baptiste, B., Courtin, A., Galoisy, L., Mathon, O., Quantin, C., Vantelon, D., Calas, G., 2023b. Mechanisms leading to exceptional niobium concentration during lateritic weathering: The key role of secondary oxides. Chem. Geol. 641, 121767. https://doi.org/10.1016/j.chemgeo.2023.121767.

Bollaert, Q., Chassé, M., Elnaggar, H., Juhin, A., Courtin, A., Galoisy, L., Quantin, C., Retegan, M., Vantelon, D., Calas, G., 2023c. Niobium speciation in minerals revealed by $L_{2,3}$-edges XANES spectroscopy. Am. Min. 108, 595–605. https://doi.org/10.2138/am-2022-8293.

Bollaert, Q., Chassé, M., Morin, G., Baptiste, B., Courtin, A., Galoisy, L., Landrot, G., Quantin, C., Calas, G., 2024. Atomic-scale environment of niobium in ore minerals as revealed by XANES and EXAFS at the Nb K-edge. Eur. J. Mineral. 36, 55–72. https://doi.org/10.5194/ejm-36-55-2024.

Braga, J.M., Biondi, J.C., 2023. Geology, geochemistry, and mineralogy of saprolite and regolith ores with Nb, P, Ba, REEs (+ Fe) in mineral deposits from the Araxá alkali-carbonatitic complex, Minas Gerais state, Brazil. J. S. Am. Earth Sci. 125, 104311. https://doi.org/10.1016/j.jsames.2023.104311.

Cao, M., Bu, H., Meng, Q., Gao, Y., 2021. Effect of surface modification by lead ions on flotation behavior of columbite-tantalite. Colloids Surf A Physicochem Eng Asp 611, 125827. https://doi.org/10.1016/j.colsurfa.2020.125827.

Carignan, J., Hild, P., Mevelle, G., Morel, J., Yeghicheyan, D., 2001. Routine Analyses of Trace Elements in Geological Samples using Flow Injection and Low Pressure On-Line Liquid Chromatography Coupled to ICP-MS: A Study of Geochemical Reference Materials BR, DR-N, UB-N, AN-G and GH. Geostand. Geoanal. Res. 25, 187–198. https://doi.org/10.1111/j.1751-908X.2001.tb00595.x.

Chakhmouradian, A.R., Reguir, E.P., Kressall, R.D., Crozier, J., Pisiak, L.K., Sidhu, R., Yang, P., 2015. Carbonatite-hosted niobium deposit at Aley, northern British Columbia (Canada): Mineralogy, geochemistry and petrogenesis. Ore Geol. Rev. 64, 642–666. https://doi.org/10.1016/j.oregeorev.2014.04.020.

Chebotarev, D.A., Doroshkevich, A.G., Klemd, R., Karmanov, N.S., 2017. Evolution of Nb-mineralization in the Chuktukon carbonatite massif, Chadobets upland (Krasnoyarsk Territory, Russia). Periodico Di Mineralogia 86. https://doi.org/10.2451/2017PM733.

Costi, H.T., 2000. Petrologia de granitos alcalinos com atlo flúor mineralizados em metais paros: o exemplo do albita-granito da mina Pitinga, Amazonas. Universidade Federal do Pará Centro de Geosciências, Belém, Brasil.

Costi, H.T., Dall'agnol, R., Moura, C.A.V., 2000. Geology and Pb-Pb Geochronology of Paleoproterozoic Volcanic and Granitic Rocks of Pitinga Province, Amazonian Craton, Northern Brazil. Int. Geol. Rev. 42, 832–849. https://doi.org/10.1080/00206810009465114.

da S. Alves, M.A., Pereira, V.P., Bastos Neto, A.C., Menegotto, E., 2018. Weathering of the Madeira world-class Sn-Nb-Ta (Cryolite, REE, U, Th) deposit, Pitinga Mine (Amazon, Brazil). J. Geochem. Explor. 186, 61–76. https://doi.org/10.1016/j.gexplo.2017.12.003.

De la Peña, F., Prestat, E., Fauske, T., Burdet, P., Lähnemann, J., Jokubauska, P., Winkler, F., 2022. hyperspy/hyperspy: Release v1.7.0.

de O. Cordeiro, P.F., Brod, J.A., Palmieri, M., de Oliveira, C.G., Barbosa, E.S.R., Santos, R. V., Gaspar, J.C., Assis, L.C., 2011. The Catalão I niobium deposit, central Brazil: Resources, geology and pyrochlore chemistry. Ore Geol. Rev. 41, 112–121. https://doi.org/10.1016/j.oregeorev.2011.06.013.

Deditius, A.P., Smith (Skomurski), F.N., Utsunomiya, S., Ewing, R.C., 2015. Role of vein-phases in nanoscale sequestration of U, Nb, Ti, and Pb during the alteration of pyrochlore. Geochim. Cosmochim. Acta 150, 226–252. https://doi.org/10.1016/j.gca.2014.11.024.

Dey, M., Mitchell, R.H., Bhattacharjee, S., Chakrabarty, A., Pal, S., Pal, S., Sen, A.K., 2021. Composition and genesis of albitite-hosted antecrystic pyrochlore from the Sevattur carbonatite complex, India. Mineral. Mag. 85, 568–587. https://doi.org/10.1180/mgm.2021.6.

Ercit, T.S., 2005. Identification and Alteration Trends of Granitic-Pegmatite-Hosted (Y, REE, U, Th)(Nb, Ta, Ti) Oxide Minerals: A Statistical Approach. Can. Mineral. 43, 1291–1303. https://doi.org/10.2113/gscanmin.43.4.1291.

Finch, A.A., McCreath, J.A., Reekie, C.D.J., Hutchison, W., Ismaila, A., Armour-Brown, A., Andersen, T., Simonsen, S.L., 2019. From Mantle to Motzfeldt: A Genetic Model for Syenite-hosted Ta, Nb-mineralisation. Ore Geol. Rev. 107, 402–416. https://doi.org/10.1016/j.oregeorev.2019.02.032.

Friis, H., Casey, W.H., 2018. Niobium Is Highly Mobile As a Polyoxometalate Ion During Natural Weathering. Can. Mineral. 56, 905–912. https://doi.org/10.3749/canmin.1800058.

Frimmel, H.E., Schedel, S., Brätz, H., 2014. Uraninite chemistry as forensic tool for provenance analysis. Appl. Geochem. 48, 104–121. https://doi.org/10.1016/j.apgeochem.2014.07.013.

Fuchs, L.H., Gebert, E., 1958. X-ray studies of synthetic coffinite, thorite and uranothorites. American Mineralogist: Journal of Earth and Planetary Materials 43, 243–248.

Gao, J., John, T., Klemd, R., Xiong, X., 2007. Mobilization of Ti–Nb–Ta during subduction: Evidence from rutile-bearing dehydration segregations and veins hosted in eclogite, Tianshan, NW China. Geochim. Cosmochim. Acta 71, 4974–4996. https://doi.org/10.1016/j.gca.2007.07.027.

Gibson, C.E., Kelebek, S., Aghamirian, M., 2015. Niobium oxide mineral flotation: A review of relevant literature and the current state of industrial operations. Int. J. Miner. Process. 137, 82–97. https://doi.org/10.1016/j.minpro.2015.02.005.
Giovannini, A.L., Mitchell, R.H., Bastos Neto, A.C., Moura, C.A.V., Pereira, V.P., Porto, C. G., 2020. Mineralogy and geochemistry of the Morro dos Seis Lagos siderite carbonatite, Amazonas. Brazil. Lithos 360–361, 105433. https://doi.org/10.1016/j.lithos.2020.105433.
Griffith, K.J., Wiaderek, K.M., Cibin, G., Marbella, L.E., Grey, C.P., 2018. Niobium tungsten oxides for high-rate lithium-ion energy storage. Nature 559, 556–563. https://doi.org/10.1038/s41586-018-0347-0.
Guastoni, A., Cámara, F., Nestola, F., 2010. Arsenic-rich fergusonite-beta-(Y) from Mount Cervandone (Western Alps, Italy): Crystal structure and genetic implications. Am. Mineral. 95, 487–494. https://doi.org/10.2138/am.2010.3239.
Guillaumont, R., Mompean, F.J., 2003. Update on the chemical thermodynamics of uranium, neptunium, plutonium, americium and technetium. Elsevier Amsterdam.
Hadlich, I.W., Bastos Neto, A.C., Pereira, V.P., 2019. The thorite mineralization in the Madeira Sn-Nb-Ta world-class deposit (Pitinga, Brazil). Ore Geol. Rev. 105, 445–466. https://doi.org/10.1016/j.oregeorev.2019.01.004.
Hadlich, I.W., 2023. Estudo integrado dos pegmatitos, da mineralização de urânio e da genthelvita no Depósito Sn-Nb-Ta (ETR, U, Th, F) Madeira (Mina Pitinga, AM): A transição magmático-hidrotermal e suas implicações metalogenéticas. Federal University of Rio Grande do Sul, Brazil.
Horbe, A.M.C., da Costa, M.L., 1999. Geochemical evolution of a lateritic Sn–Zr–Th–Nb–Y–REE-bearing ore body derived from apogranite: the case of Pitinga, Amazonas — Brazil. J. Geochem. Explor. 66, 339–351. https://doi.org/10.1016/S0375-6742(99)00002-3.
Janeczek, J., Ewing, R.C., 1992. Structural formula of uraninite. J. Nucl. Mater. 190, 128–132. https://doi.org/10.1016/0022-3115(92)90082-V.
Khan, A., Faisal, S., Ullah, Z., Ali, L., Ghaffari, A., Nawab, J., Rashid, M.U., 2021. Pyrochlore-group minerals from the Loe-Shilman Carbonatite Complex, NW Pakistan: implications for evolution of carbonatite system. Periodico di Mineralogia Vol. 90 No. 2 (2021): In progress. https://doi.org/10.13133/2239-1002/17360.
Kotova, N.P., 2012. Experimental study of concentration dependence of niobium oxide solubility in fluoride solutions at T= 550°C, P= 500 bar and low oxygen fugacity (Co-CoO buffer). Vestn. Otd. Nauk Zemle 4. https://doi.org/10.2205/2012NZ_ASEMPG.
Lenharo, S.L.R., Pollard, P.J., Born, H., 2003. Petrology and textural evolution of granites associated with tin and rare-metals mineralization at the Pitinga mine, Amazonas, Brazil. Lithos 66, 37–61. https://doi.org/10.1016/S0024-4937(02)00201-3.
Lian, J., Zhang, J.M., Pointeau, V., Zhang, F.X., Lang, M., Lu, F.Y., Poinssot, C., Ewing, R. C., 2009. Response of synthetic coffinite to energetic ion beam irradiation. J. Nucl. Mater. 393, 481–486. https://doi.org/10.1016/j.jnucmat.2009.07.005.
Liu, H., Ding, X., Yan, H., Liu, K., Liu, J., Huang, X., 2024. The solubility and complexation of Niobium in hydrothermal fluids. Solid Earth Sciences 9, 1–16. https://doi.org/10.1016/j.sesci.2023.12.001.
Lukyanova, E.V., Akinfiev, N.N., Zotov, A.V., Rass, I.T., Kotova, N.P., Korzhinskaya, V.S., 2017. Niobium in hydrothermal systems related to alkali granites: Thermodynamic description of hydroxo and hydroxofluoride complexes. Geol. Ore Deposits 59, 305–314. https://doi.org/10.1134/S1075701517040031.
Lumpkin, G.R., Ewing, R.C., 1995. Geochemical alteration of pyrochlore group minerals; pyrochlore subgroup. Ameircan Mineralogist 80, 732–743. https://doi.org/10.2138/am-1995-7-810.
Macmillan, E., Cook, N.J., Ehrig, K., Pring, A., 2017. Chemical and textural interpretation of late-stage coffinite and brannerite from the Olympic Dam IOCG-Ag-U deposit. Mineral. Mag. 81, 1323–1366. https://doi.org/10.1180/minmag.2017.081.006.
Melgarejo, J.C., Costanzo, A., Bambi, A.C.J.M., Gonçalves, A.O., Neto, A.B., 2012. Subsolidus processes as a key factor on the distribution of Nb species in plutonic carbonatites: The Tchivira case, Angola. Lithos 152, 187–201. https://doi.org/10.1016/j.lithos.2012.06.024.
Migdisov, A., Williams-Jones, A.E., Brugger, J., Caporuscio, F.A., 2016. Hydrothermal transport, deposition, and fractionation of the REE: Experimental data and thermodynamic calculations. Chem. Geol. 439, 13–42. https://doi.org/10.1016/j.chemgeo.2016.06.005.
Minuzzi, O.R.R., Neto, A.C.B., Antonio, J., Flores, A., Pereira, V.P., 2005. O depósito crilotítico maciço e o minério disseminado de criolita da mina Pitinga (Amazonas, Brasil). Revista Brasileira De Geociências 35, 101–121. https://doi.org/10.25249/0375-7536.200636S1104123.
Mitchell, R.H., 2015. Primary and secondary niobium mineral deposits associated with carbonatites. Ore Geol. Rev. 64, 626–641. https://doi.org/10.1016/j.oregeorev.2014.03.010.
Nasraoui, M., Bilal, E., 2000. Pyrochlores from the Lueshe carbonatite complex (Democratic Republic of Congo): a geochemical record of different alteration stages. J. Asian Earth Sci. 18, 237–251. https://doi.org/10.1016/S1367-9120(99)00056-5.
Newville, M., 2013. Larch: An Analysis Package for XAFS and Related Spectroscopies. J. Phys. Conf. Ser. 430, 012007. https://doi.org/10.1088/1742-6596/430/1/012007.
Palmieri, M., Brod, J.A., Cordeiro, P., Gaspar, J.C., Barbosa, P.A.R., de Assis, L.C., Junqueira-Brod, T.C., Silva, S.E., Milanezi, B.P., Machado, S.A., Jácomo, M.H., 2022. The Carbonatite-Related Morro do Padre Niobium Deposit, Catalão II Complex, Central Brazil. Econ. Geol. 117, 1497–1520. https://doi.org/10.5382/econgeo.4951.
Pearson, R.G., 1963. Hard and soft acids and bases. J. Am. Chem. Soc. 85, 3533–3539. https://doi.org/10.1021/ja00905a001.
Peiffert, C., Cuney, M., 1996. Uranium in granitic magmas: Part 2. Experimental determination of uranium solubility and fluid-melt partition coefficients in the uranium oxide-haplogranite-H_2O-NaX (X= Cl, F) system at 770 C, 2 kbar. Geochim. Cosmochim. Acta 60, 1515–1529. https://doi.org/10.1007/s10953-010-9495-z.
Peiffert, C., Nguyen-Trung, C., Palmer, D.A., Laval, J.P., Giffaut, E., 2010. Solubility of B-Nb_2O_5 and the Hydrolysis of Niobium(V) in Aqueous Solution as a Function of Temperature and Ionic Strength. J. Solution. Chem. 39, 197–218.
Pöml, P., Menneken, M., Stephan, T., Niedermeier, D.R.D., Geisler, T., Putnis, A., 2007. Mechanism of hydrothermal alteration of natural self-irradiated and synthetic crystalline titanate-based pyrochlore. Geochim. Cosmochim. Acta 71, 3311–3322. https://doi.org/10.1016/j.gca.2007.03.031.
Rajak, D.K., Jordaan, R., Gómez-Arias, A., Purcell, W., 2022. Extractive metallurgy of columbite-tantalite ore: A detailed review. Miner. Eng. 190, 107917. https://doi.org/10.1016/j.mineng.2022.107917.
Ribeiro da Costa, I., Roseiro, J., Figueiras, J., Rodrigues, P.C.R., Mateus, A., 2021. Pyrochlore from the Bailundo Carbonatite Complex (Angola): Compositional variation and implications to mineral exploration. J. Afr. Earth Sc. 177, 104154. https://doi.org/10.1016/j.jafrearsci.2021.104154.
Salvi, S., Williams-Jones, A.E., Linnen, R.L., Samson, I.M., 2005. Alkaline granite-syenite deposits. Rare-Element Geochemistry and Mineral Deposits 17, 315–341.
Schaefers, F., Mertin, M., Gorgoi, M., 2007. KMC-1: A high resolution and high flux soft x-ray beamline at BESSY. Rev. Sci. Instrum. 78, 123102. https://doi.org/10.1063/1.2808334.
Schulz, Klaus.J., Piatak, Nadine.M., Papp, John.F., 2017. Niobium and tantalum (No. 1802– M). US Geological Survey.
Sheard, E.R., Williams-Jones, A.E., Heiligmann, M., Pederson, C., Trueman, D.L., 2012. Controls on the Concentration of Zirconium, Niobium, and the Rare Earth Elements in the Thor Lake Rare Metal Deposit, Northwest Territories, Canada. Econ. Geol. 107, 81–104. https://doi.org/10.2113/econgeo.107.1.81.
Shikika, A., Sethurajan, M., Muvundja, F., Mugumaoderha, M.C., 2020. A review on extractive metallurgy of tantalum and niobium. Hydrometall. 198, 105496. https://doi.org/10.1016/j.hydromet.2020.105496.
Smith, M., Kynicky, J., Xu, C., Song, W., Spratt, J., Jeffries, T., Brtnicky, M., Kopriva, A., Cangelosi, D., 2018. The origin of secondary heavy rare earth element enrichment in carbonatites: Constraints from the evolution of the Huanglongpu district, China. Lithos 308, 65–82. https://doi.org/10.1016/j.lithos.2018.02.027.
Smith, M.P., Spratt, J., 2012. The chemistry of niobium mineralisation at Bayan Obo, Inner Mongolia, China: Constraints on the hydrothermal precipitation and alteration of Nb-minerals. Acta Geol. Sin. 86, 700–722.
Szenknect, S., Mesbah, A., Cordara, T., Clavier, N., Brau, H.-P., Le Goff, X., Poinssot, C., Ewing, R.C., Dacheux, N., 2016. First experimental determination of the solubility constant of coffinite. Geochim. Cosmochim. Acta 181, 36–53. https://doi.org/10.1016/j.gca.2016.02.010.
Szenknect, S., Alby, D., López García, M., Wang, C., Podor, R., Miserque, F., Mesbah, A., Duro, L., Zetterström Evins, L., Dacheux, N., 2020. Coffinite formation from UO_{2+x}. Sci. Rep. 10, 12168. https://doi.org/10.1038/s41598-020-69161-1.
Timofeev, A., Migdisov, A.A., Williams-Jones, A.E., 2015. An experimental study of the solubility and speciation of niobium in fluoride-bearing aqueous solutions at elevated temperature. Geochim. Cosmochim. Acta 158, 103–111. https://doi.org/10.1016/j.gca.2015.02.015.
Timofeev, A., Williams-Jones, A.E., 2015. The Origin of Niobium and Tantalum Mineralization in the Nechalacho REE Deposit, NWT, Canada. Econ. Geol. 110, 1719–1735. https://doi.org/10.2113/econgeo.110.7.1719.
Tremblay, J., Bédard, L.P., Matton, G., 2017. Columbitization of fluorcalciopyrochlore by hydrothermalism at the Saint-Honoré alkaline complex, Québec (Canada): New insights on halite in carbonatites. Ore Geol. Rev. 91, 695–707. https://doi.org/10.1016/j.oregeorev.2017.08.027.
Van Lichtervelde, M., Grand'Homme, A., de Saint-Blanquat, M., Olivier, P., Gerdes, A., Paquette, J.-L., Melgarejo, J.C., Druguet, E., Alfonso, P., 2017. U-Pb geochronology on zircon and columbite-group minerals of the Cap de Creus pegmatites, NE Spain. Mineral. Petrol. 111, 1–21. https://doi.org/10.1007/s00710-016-0455-1.
Vantelon, D., Trcera, N., Roy, D., Moreno, T., Mailly, D., Guilet, S., Metchalkov, E., Delmotte, F., Lassalle, B., Lagarde, P., Flank, A.-M., 2016. The LUCIA beamline at SOLEIL. J. Synchrotron Radiat. 23, 635–640. https://doi.org/10.1107/S1600577516000746.
Velásquez-Ruiz, F., Reich, M., Broom-Fendley, S., Beard, C.D., Barra, F., Romero, R., Cordeiro, P., 2024. Origin of carbonatite-related niobium deposits: Insights from pyrochlore geochemistry. Geochim. Cosmochim. Acta 366, 1–16. https://doi.org/10.1016/j.gca.2023.12.010.
Verwoerd, W.J., Viljoen, E.A., Chevallier, L., 1995. Rare metal mineralization at the Salpeterkop carbonatite complex, Western Cape Province, South Africa. J. Afr. Earth Sc. 21, 171–186. https://doi.org/10.1016/0899-5362(95)00085-8.
Wall, F., Williams, C.T., Woolley, A.R., Nasraoui, M., 1996. Pyrochlore from Weathered Carbonatite at Lueshe. Zaire. Mineral. Mag. 60, 731–750. https://doi.org/10.1180/minmag.1996.060.402.03.
Walter, B.F., Parsapoor, A., Braunger, S., Marks, M.A.W., Wenzel, T., Martin, M., Markl, G., 2018. Pyrochlore as a monitor for magmatic and hydrothermal processes in carbonatites from the Kaiserstuhl volcanic complex (SW Germany). Chem. Geol. 498, 1–16. https://doi.org/10.1016/j.chemgeo.2018.08.008.
Wang, K., Wang, L.-X., Ma, C.-Q., Zhu, Y.-X., She, Z.-B., Deng, X., Chen, Q., 2021. Mineralogy and geochemistry of the Zhuxi Nb-rich trachytic rocks, South Qinling (China): Insights into the niobium mineralization during magmatic-hydrothermal processes. Ore Geol. Rev. 138, 1–21. https://doi.org/10.1016/j.oregeorev.2021.104346.
Wertich, V., Kubeš, M., Leichmann, J., Holá, M., Haifler, J., Mozola, J., Hršelová, P., Jaroš, M., 2022. Trace element signatures of uraninite controlled by fluid-rock interactions: A case study from the Eastern Moldanubicum (Bohemian Massif). J. Geochem. Explor. 243, 107111. https://doi.org/10.1016/j.gexplo.2022.107111.

Williams-Jones, A.E., Vasyukova, O.V., 2022. Niobium, Critical Metal, and Progeny of the Mantle. Econ. Geol. https://doi.org/10.5382/econgeo.4994.

Wu, B., Hu, Y.-Q., Bonnetti, C., Xu, C., Wang, R.-C., Zhang, Z.-S., Li, Z.-Y., Yin, R., 2021. Hydrothermal alteration of pyrochlore group minerals from the Miaoya carbonatite complex, central China and its implications for Nb mineralization. Ore Geol. Rev. 132, 104059. https://doi.org/10.1016/j.oregeorev.2021.104059.

Wu, H., Huang, H., Zhang, Z., Wang, T., Guo, L., Gao, Y., Zhang, Z., 2023. Highly differentiated trachytic magma linked with rare metal mineralization: A case study from the Shuanghekou Nb deposit, South Qinling. Lithos 438, 106990.

Wyckoff, R.W.G., 1963. Crystal structures. Interscience publishers New York.

Xiang, Y.-X., Yang, J.-H., Chen, J.-Y., Zhang, Y., 2017. Petrogenesis of Lingshan highly fractionated granites in the Southeast China: Implication for Nb-Ta mineralization. Ore Geol. Rev. 89, 495–525. https://doi.org/10.1016/j.oregeorev.2017.06.029.

Xu, H., Wang, Y., Zhao, P., Bourcier, W.L., Konynenburg, R.V., Shaw, H.F., 2004. Investigation of Pyrochlore-Based U-Bearing Ceramic Nuclear Waste: Uranium Leaching Test and TEM Observation. Environ. Sci. Tech. 38, 1480–1486. https://doi.org/10.1021/es030582v.

Yajima, T., 1994. Solubility Measurements of Uranium and Niobium, Nuclear Engineering Research Laboratory. Faculty of Engineering Univeristy of Tokyo, Yayoi Kenkyuukai Report, UTNL, pp. 127–143.

Yan, S., Niu, H.-C., Zhao, X., Zhang, Q.-B., Zhang, H.-J., Zhao, X.-C., 2022. Rare metal enrichment of the Tianbao trachytic complex, North Daba Mountains (south Qinling): Insights from textures and geochemistry of trachytes and Nb-REE minerals. Ore Geol. Rev. 146, 104948. https://doi.org/10.1016/j.oregeorev.2022.104948.

Yang, Z.-Y., Wang, R.-C., Che, X.-D., Harlov, D., 2023. Restrictions on Niobium enrichment by alteration of Niobium-rich biotite in pure water, acid, alkaline and fluoride-bearing solutions at 200 MPa and 300–600° C. Geochim. Cosmochim. Acta 343, 115–132. https://doi.org/10.1016/j.gca.2022.12.031.

Yin, R., 2023. Zircons in NYF-type pegmatites in the Emeishan large igneous province, SW China: A record of Nb and REE mineralization processes. Ore Geol. Rev. 162, 1–15. https://doi.org/10.1016/j.oregeorev.2023.105700.

Ying, Y.-C., Chen, W., Chakhmouradian, A.R., Zhao, K.-D., Jiang, S.-Y., 2023. Textural and compositional evolution of niobium minerals in the Miaoya carbonatite-hosted REE-Nb deposit from the South Qinling Orogen of central China. Miner. Deposita 58. https://doi.org/10.1007/s00126-022-01126-y.

Yong, T., Linnen, R.L., McNeil, A.G., 2022. An Experimental Study of Pyrochlore Solubility in Peralkaline Granitic Melts. Econ. Geol. 118, 209–223. https://doi.org/10.5382/econgeo.4958.

Zaitsev, A.N., Chakhmouradian, A.R., Siidra, O.I., Spratt, J., Williams, C.T., Stanley, C.J., Petrov, S.V., Britvin, S.N., Polyakova, E.A., 2011. Fluorine-, yttrium- and lanthanide-rich cerianite-(Ce) from carbonatitic rocks of the Kerimasi volcano and surrounding explosion craters, Gregory Rift, northern Tanzania. Mineral. Mag. 75, 2813–2822. https://doi.org/10.1180/minmag.2011.075.6.2813.

Zaitsev, A.N., Spratt, J., Shtukenberg, A.G., Zolotarev, A.A., Britvin, S.N., Petrov, S.V., Kuptsova, A.V., Antonov, A.V., 2021. Oscillatory- and sector-zoned pyrochlore from carbonatites of the Kerimasi volcano, Gregory rift, Tanzania. Mineral. Mag. 85, 532–553. https://doi.org/10.1180/mgm.2020.101.

Zanetta, P.-M., Le Guillou, C., Leroux, H., Zanda, B., Hewins, R.H., Lewin, E., Pont, S., 2019. Modal abundance, density and chemistry of micrometer-sized assemblages by advanced electron microscopy: application to chondrites. Chem. Geol. 514, 27–41. https://doi.org/10.1016/j.chemgeo.2019.03.025.

Zhang, L., Jiang, S.-Y., Romer, R.L., Su, H.-M., 2023. Relative importance of magmatic and hydrothermal processes for economic Nb-Ta-W-Sn mineralization in a peraluminous granite system: The Zhaojinggou rare-metal deposit, northern China. Bulletin 135, 2529–2553. https://doi.org/10.1130/B36503.1.

Zhao, Z., Yang, X., Lu, S., Lu, Y., Sun, C., Chen, S., Zhang, Z., Bute, S.I., Zhao, L., 2021. Genesis of Late Cretaceous granite and its related Nb–Ta–W mineralization in Shangbao, Nanling Range: Insights from geochemistry of whole-rock and Nb–Ta minerals. Ore Geol. Rev. 131. https://doi.org/10.1016/j.oregeorev.2020.103975.

Zhu, Y., Wang, L., Pan, Y., Zhang, C., Almeev, R.R., She, Z., Holtz, F., 2024. Pyrochlore composition and Sm-Nd isotope signature as indicators of magmatic-hydrothermal processes: The case of Ririwai complex, north-Central Nigeria. Chem. Geol. 652. https://doi.org/10.1016/j.chemgeo.2024.122021.

Zozulya, D., MacDonald, R., Bagiński, B., 2020. REE fractionation during crystallization and alteration of fergusonite-(Y) from Zr-REE-Nb–rich late- to post-magmatic products of the Keivy alkali granite complex. NW Russia. Ore Geology Reviews 125. https://doi.org/10.1016/j.oregeorev.2020.103693.